PROCSIMA: Diffractionless Beamed Propulsion for Breakthrough Interstellar Missions

NIAC Phase I Report

Christopher Limbach and Ken Hara

March 25, 2019

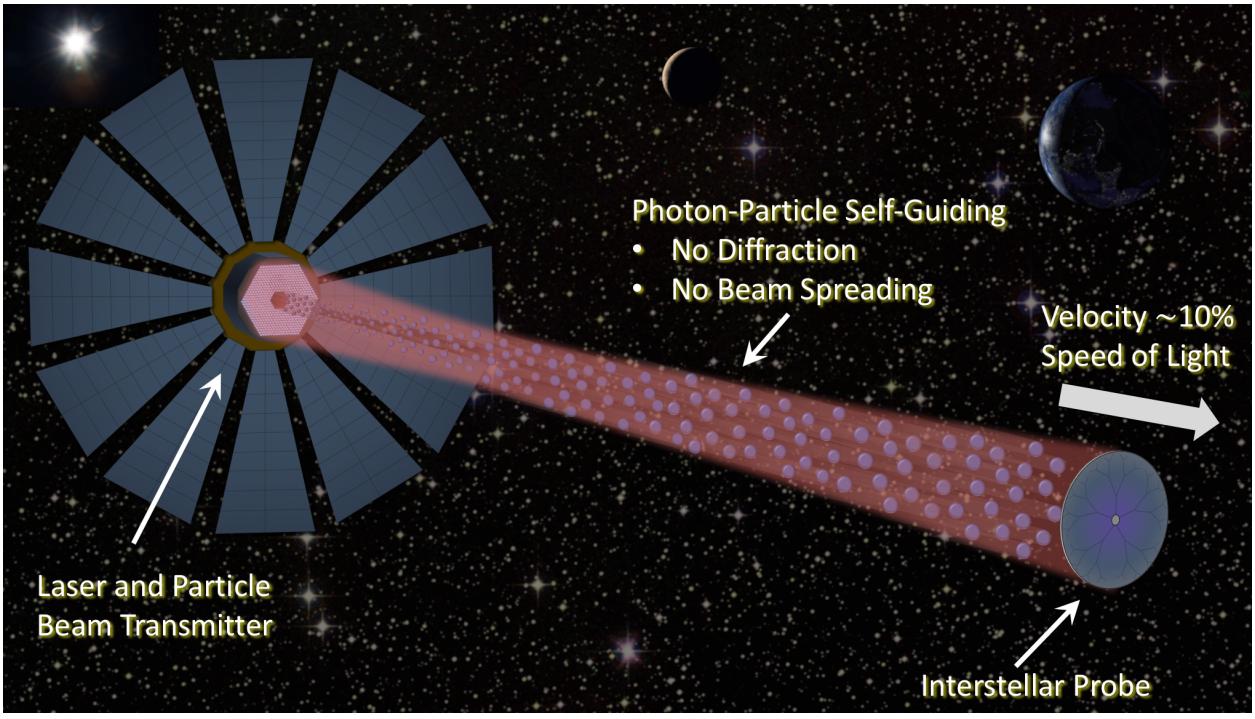

Executive Summary

The following report describes a new propulsion concept based on self-guiding of a combined light and particle beam and explores the physics, technology and design principles needed to implement such a system for an interstellar fly-by mission to Proxima b. While the relevant self-focusing mechanism has been considered in an optical context, this is the first application to space propulsion known to the authors. The purpose of the present study is to provide a broad overview of the pertinent physics and design principles, credibly assess propulsion capabilities, and lay a comprehensive foundation for further, more targeted investigations of critical system elements and processes.

Starting from basic principles, this report describes the equations of motion and physical phenomena needed to establish the feasibility of self-guiding and furthermore analyze the production and sustainment of the self-guided beam. Compared with laser or particle beam propulsion alone, the self-guided beam concept introduces a plethora of light-matter interactions and additional complexities, imposing certain constraints on the geometric and physical characteristics of the beam sources. In particular, we have the identified the particle beam as a crucial element of the proposed concept. System constraints are quantitatively analyzed and then explored by developing and applying a mission design process to a Proxima b flyby mission as well as a nearer-term mission to the solar gravitational lens point.

Through this study, we conclude that propulsion by self-guided beams is credible based on an analysis of the governing equations and literature review. A quantitative analysis of phenomena including light scattering/absorption, photo-ionization, heating, collisions, gravity, reference-frame effects, and beam riding revealed no "show-stoppers". Missions design indicates that propulsion capability is strongly affected by 1) the particle beam source characteristics, specifically a parameter known as *brightness*, and 2) power constraints and mission constraints on the final velocity. An analysis of the Proxima b mission demonstrated that while self-guided beamed propulsion enables a $0.1c$ fly-by with a 5 gram probe, a larger 0.6 kilogram payload is obtained for a $0.075c$ mission. Both optimizations were performed for 50 GW of available beam power and a transmitter area of only 1 m^2, the latter a reduction of $> 10^6$ relative to comparable laser propulsion concepts. Observed payload mass scaling with velocity to the power of ~ 8.8 results in dramatic improvements for slightly extended mission duration, and suggests game-changing capability for near-term low velocity missions throughout the solar system.

Acknowledgements

The authors gratefully acknowledge support from NASA, in particular the NIAC program office, as well as helpful feedback and constructive criticisms from NIAC fellows and colleagues in academia and industry.

Contents

1 Introduction 8
1.1 Proposed Concept and Scope 9
1.2 Beamed Propulsion 10
1.3 Beamed Propulsion Dynamics 13

2 Self-Guided Beam Physics 16
2.1 Literature Review 16
2.2 Physical Basis for Self-Guiding 16
2.2.1 Light Guiding Mechanism 17
2.2.2 The Dipole Force and Stochastic Heating 19
2.2.3 Particle Dynamics 21
2.2.4 Trapped Fraction 22
2.3 Loss Processes and Destruction of Self-Guiding 23
2.3.1 Rayleigh Scattering 24
2.3.2 Collisions 25
2.3.3 Multi-Photon Ionization 27
2.3.4 Gravity and Fictitious Forces 29
2.3.5 Transmitter Location and Beam Riding 32

3 Mission Design 34
3.1 Brightness: A Key Parameter 34
3.2 Optimization Framework for Self-Guided Beamed Propulsion 35
3.3 Proxima b Flyby Mission 36
3.4 Solar Gravity Lens Mission 38

4 Numerical Simulation 41
4.1 Beam Propagation 42
4.2 Verification 42
4.3 Particle and Coupled Simulation 44

5 Particle Beam Technology 45
5.1 Bright Atomic Beams 45
5.2 High Current, High Energy Beams 46
5.3 Neutral Beams 47
5.4 Technology Development Recommendations 48

6 Conclusion 50

A Area - Divergence Product 51

B Paraxial Wave Equation Derivation 52

Bibliography 54

Symbols and Abbreviations

PROCSIMA	Photon-paRticle Optically Coupled Soliton Interstellar Mission Accelerator
c	speed of light
I_{sp}	specific impulse
A_t	transmitter cross sectional area
A_{sc}	spacecraft cross sectional area
Ω	beam divergence solid angle
Π	area - divergence product
ϵ	beam emittance
L	beam propagation distance, acceleration distance
λ	laser wavelength in transmitter frame
$\theta_{1/2}$	beam divergence half-angle
k_b	Boltzmann constant
$T_\perp$	transverse temperature
D	transmitter diameter
E_k	particle kinetic energy
v_b	particle beam velocity
m_a	atomic mass
w_0	beam waist of a Gaussian beam
z_r	confocal beam parameter
h	Planck constant
$\hbar$	reduced Planck constant
Γ	decay rate
k	propagation constant
T_d	Doppler temperature
T_r	recoil temperature
R_L	optical reflectance
R_p	particle reflection coefficient
P_L	laser beam power
P_p	particle beam power
T_L	laser beam thrust
T_p	particle beam thrust
v_{sc}	spacecraft velocity
β	spacecraft velocity normalized to c
$\dot{m}$	mass flow rate
m_{sc}	spacecraft mass
v_t	thermal velocity
ϵ_0	permittivity of free space
μ_0	permeability of free space
N	particle number density
$\mathbf{r}$	position vector
I_L	laser intensity
Z_0	impedance of free space
A_p	particle beam area

A_L	laser beam area
λ_{dB}	deBroglie wavelength
$\mathbf{d}$	electric dipole moment
$\mathbf{E}$	electric field
α_v	polarizability volume
k_0	propagation constant in vacuum
i	$\sqrt{-1}$
∇	del operator
V	waveguide V-parameter
η	refractive index
$\delta\eta$	refractive index contrast
K	self-focusing constant
f_{0j}	oscillator strength
λ'	Doppler shifted wavelength
F	force
U	dipole potential
R_{sc}	scattering rate
Δ	angular frequency detuning
σ_R	total Rayleigh scattering cross section
$\dot{T}$	time rate of change in temperature
t_h	stochastic heating time constant
$\mathbf{v}$	vector velocity
t	time
f	phase space distribution function
VDF	velocity distribution function
S	collision term
w_L	laser beam width
r_n	neutral particle beam width
F_{trap}	fraction of trapped particles at a point
F_{net}	total (net) fraction of particles trapped
n_0	solar wind density at 1 AU
σ_{pn}	proton-neutral collision cross section
σ_{nn}	neutral-neutral collision cross section
λ_{mfp}	mean free path
τ_c	collision time
d_c	collision distance, interval
a	scattering length
γ	Keldysh parameter
U_i	ionization energy
I_c	characteristic current
ω	angular frequency (of laser)
m_e	electron mass
e	fundamental charge
τ_i	ionization time
σ_{N_k}	multi-photon ionization cross section

MPI	multi-photon ionization
w_i	multi-photon ionization rate
N_k	number of photons needed to ionize
R_c	radius of curvature
$a_\perp$	acceleration perpendicular to beam
S	bend sensitivity parameter
$\delta\eta_{eff}$	effective refractive index
Ω	angular orbital frequency
a_{br}	beam-riding acceleration
δv	velocity change
Δr	grid size in r
Δz	step size in z
B	particle beam brightness
v_f	final velocity
ψ	Guoy phase shift
B	magnetic field
ϵ	permittivity
FIB	focused ion beam
V_m	maximum voltage
V_i	intermediate voltage

Unit Abbreviations

sec	second
asec	arc second
kg	kilogram
W	watt
Ly	lightyear
A	amp
m	meter
eV	electron volt
K	Kelvin
Ω	Ohm
AU	astronomical unit
sr	steradian

1 Introduction

The recent discovery of numerous earth-sized planets around other stars, such as Proxima b (4.24 Ly [1]) and Barnard's star b (5.96 Ly [2]), has excited the space community and generated intense study of interstellar mission concepts by NASA and private foundations [3, 4, 5, 6, 7]. Closer destinations, such as the gravitational lens point, Kuiper belt object, and interstellar interlopers such as asteroid 'Oumuamua are also of great scientific interest. However, all such missions challenge existing propulsion technologies due to the tremendous speed, energy, power and specific impulse required. Innovative propulsion solutions are needed to enable these high-energy missions under the constraints of available power and space infrastructure [3].

Figure 1 summarizes an array of propulsion options currently under investigation. Nuclear propulsion [8, 9, 10, 11, 12], light ion engines [13] and beamed propulsion all provide specific impulse above 10,000 sec, enabling the fast outer solar system missions described above. Beam concepts are unique in that their propulsion capability principally derives from the separation of power and propulsion subsystems from the spacecraft itself, thereby liberating the propulsion dynamics from the rocket equation. An additional corollary is that the beam system may be much more massive, complex and therefore capable than on-board thrusters. It is the potential for more complex systems that enable, *in principle*, the throttling of particle beam specific impulse and thrust over the wide range shown in Fig. 1 (dashed lines) as well as the low divergence and high thrust needed for effective acceleration of large payloads.

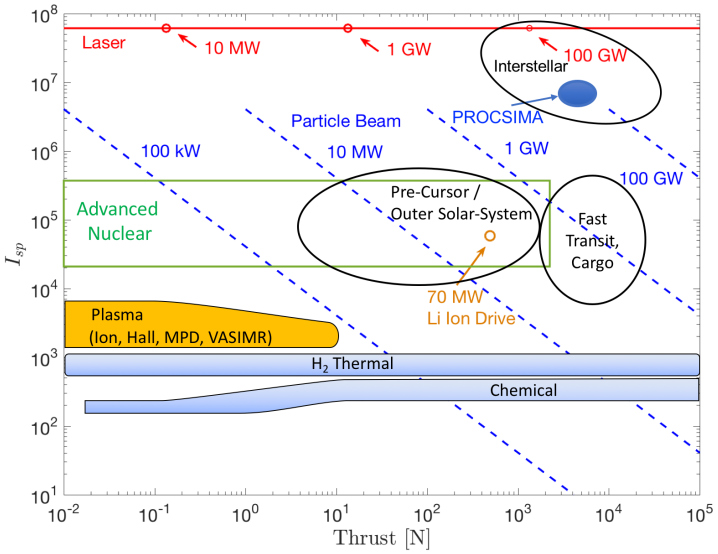

Figure 1: Beamed and other propulsion technologies.

Coupled with a light weight space probe, a particle beam with $I_{sp} > 10^6$ sec would be ideally suited to interstellar missions, with higher thrust-to-power ratio than laser propulsion. Unlike advanced nuclear [8, 9, 10, 11, 12] and ion propulsion systems (e.g. Li ion direct drive [13]), particle beam I_{sp} is not constrained by the mass or complexity of the beam system nor the chemical or nuclear energy content of the fuel. Other missions, such as interstellar precursor missions and fast cargo transport around the solar system, can also be achieved by high power particle beam systems.

The cost of avoiding the rocket equation, as compared with reaction engines, is the finite acceleration time afforded in beamed propulsion, a consequence of the finite divergence of both laser and particle beams. The problem is illustrated in Fig. 2, which shows a schematic of three beamed propulsion concepts, using (A) laser beam only, (B) particle beam only, and (C) the proposed concept: a self-guided beam. During propagation of a laser or particle

beam, its transverse extent increases with distance, reducing thrust and energy efficiency. This can occur either by diffraction (in the case of laser propulsion) or due to thermal motions perpendicular to the beam (in the case of particle beams). A primary driver in all beamed propulsion is therefore to minimize the beam divergence, which for lasers entails large space infrastructure such as kilometer-scale laser arrays [14, 5, 4]. **The central problem addressed by the proposed concept is the limitation of beamed propulsion due to beam divergence.**

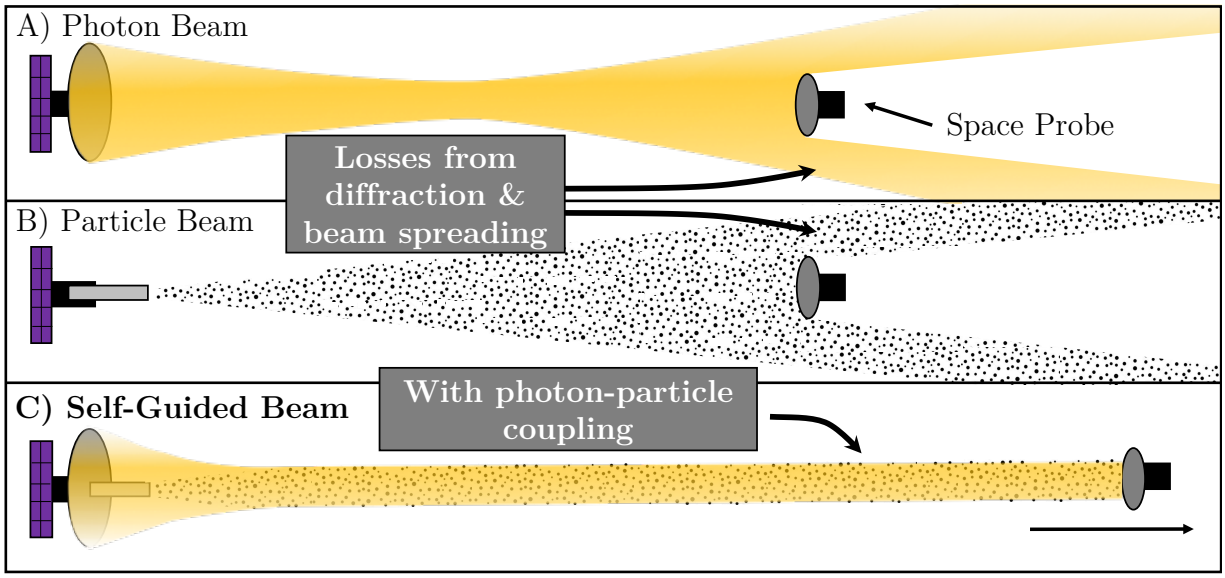

Figure 2: Beam concepts compared: a) laser propulsion, b) mass beam propulsion, c) PROCSIMA (self-guided beam) concept.

1.1 Proposed Concept and Scope

This report describes a new propulsion concept for interstellar and high velocity missions based on combined laser and particle beams. This approach, shown in Fig. 2c, exploits a mutual self-guiding effect, derived from optical forces and focusing, to overcome and eliminate divergence. The physical mechanism for self-guiding invoked here was first analyzed by Askar'yan [15], and has been subsequently described as laser self-guiding, self-trapping, "back-action" or opto-mechanical coupling between the light and particle beams [15, 16, 17, 18, 19, 20].

If successful, this technology will 1) increase acceleration distance and reduce g-loading on future space probes, 2) reduce the necessary transmitter aperture and space infrastructure for beamed propulsion, and 3) increase payload due to extended acceleration distance and high thrust-to-weight of the particle beam. The objective of Phase I has been to investigate the above claims, develop evidence for their support for refutation, determine beam system requirements, and assess the concept's unknowns and potential for space propulsion.

The main contributions and highlights in Phase I are mirrored in the sections of the following report, and include:

1. Framing of self-guided beamed propulsion in the context of both laser and particle

beam propulsion (Sec. 1.2).

2. Development of the governing equations and enumeration of assumptions for analysis of the self-guided beam, including an understanding of self-guiding in the context of classical electromagnetism and beam thermodynamics (Sec. 2.2).

3. Analysis of relevant physical processes and the limits imposed thereby, including Rayleigh scattering, stochastic heating, multi-photon ionization, and gravitational and reference frame effects (Sec. 2.3).

4. Development of a beam parameter optimization and design framework to assess performance over a range of missions, in particular a fly-by mission of Proxima b (Sec. 3).

5. Exploratory studies of field and particle solvers for uncoupled, axisymmetric beam propagation (Sec. 4).

6. Establishment of performance metrics for the particle beam source, in the context of existing technologies, and their impact on propulsion capability (Sec. 3,5).

In the following sections, we begin by framing this new concept in the existing literature on beamed propulsion and optical self-guiding.

1.2 Beamed Propulsion

While the current status of laser and particle beam concepts can be found in recent papers [5] and reviews [21], we aim to offer here a unified description of the similar challenges and fundamental limitations of beamed propulsion concepts. In particular, we attempt to draw parallels and comparisons between particle beams, which have received relatively less scrutiny, and laser approaches, which have been considered for some time [22, 23, 25, 26, 28].

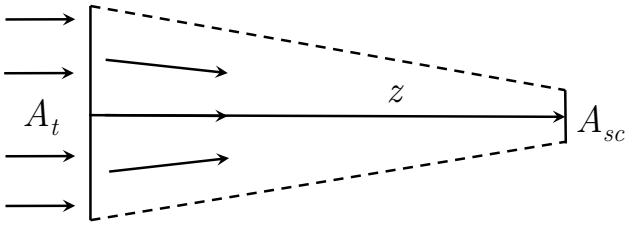

Figure 3: Generic beamed propulsion problem.

In both approaches, a beam of initial size A_t is transmitted into space and focused at a target spacecraft of finite area A_{sc} at a distance z, as shown in Fig. 3. This process, **in both particle and light optics**, is governed by a fundamental conservation law variously known as the law of sines or Abbe sine law or the law of Helmholtz-Lagrange, and is related to the optical concepts of beam parameter product and etendue [29, 30, 31]. As noted by McClelland [29], *"This law can be derived from thermodynamic principles, and ultimately stems from Liouville's theorem on the conservation of phase space volume in the presence of a conservative potential"*. In all embodiments, this principle states that the phase space volume [i] of the beam is conserved under the action of conservative forces or optical elements. The practical implication is that one property

[i] Here, phase space volume refers to the position-momentum space, or equivalently, position-angle space, transverse to the propagation direction.

of the beam, the product of the beam area A and ray bundle divergence Ω, remains constant during propagation [ii]:

$$A\Omega = \Pi = \text{constant}. \quad (1)$$

The area-divergence product Π is a fundamental property of the beam system and in particle beam optics is proportional to $\epsilon_x \epsilon_y$, where ϵ is known as emittance [32, 33]. Physically, Π measures of the transverse phase-space volume of the beam and can furthermore be associated with its entropy [34].

In Appendix 7, we derive an expression for the maximum distance a beam can be focused to a spot A_{sc}, which is the spacecraft capture area,

$$L = \sqrt{\frac{A_t A_{sc}}{\Pi}}. \quad (2)$$

Eq. 2 is valid for both laser and particle beams described by their parameter Π and focused by conservative (linear) optical elements (e.g. optical lenses an electrostatic lens) or combined by a coherent phased array of smaller sources. The importance of maximizing the distance L, or equivalently the time spent on the beam, was first noted by Marx [25]. From Eq. 2 we see that one option, widely noted by early photon propulsion proposals, is maximizing the transmitter or receiver area (e.g. Sanger [22, 23], Marx [25], Redding [26], and Forward [28, 35]) and continues to drive designs by the Breakthrough Starshot Initiative [6] and recent studies by Lubin [14] and Parkin [4]. For laser beams, $\Pi = \lambda^2$ is fixed by the laser wavelength and a typical value is $\Pi = 10^{-12}$ m^2 [iii]. Thus, maximizing the transmitter and capture areas is the only option for improving L, other than reduced wavelength.

Mass beam studies have also focused on increasing beam time by maximizing the capture area, for example, in the Starwisp concept [35]). However, most research efforts have focused on either 1) reducing Π, specifically the divergence Ω, using laser cooling [37], or 2) overcoming Π by employing guiding elements, such as beacons (Kare [38]), nanotechnology (i.e. smart pellets, [39]), laser ablation systems [22, 37], and other concepts [21].

For particles, rather than Π, it is more useful to consider the temperature of the beam atoms in the moving reference frame. In general, we consider the possibility that the axial (longitudinal) temperature given by $T_{||}$ is different from the transverse (perpendicular) temperature given by $T_{\perp}$. The divergence is then given by,

$$\Omega = \pi\theta_{1/2}^2 = \frac{\pi}{2}\frac{k_b T_{\perp}}{E_k}, \quad (3)$$

[ii] Note that the divergence Ω refers to the angular spread of the rays passing through a point in the beam, rather than the convergence/divergence angle of the beam as a whole.

[iii] This is exact for a Gaussian beam, where $A = \pi w_0^2$ and $\Omega = \pi w_0^2 / z_r^2$, where w_0 is the beam waist and z_r is the confocal beam parameter [36]

where $\theta_{1/2} = \frac{v_t}{v_b}$ is the divergence half-angle and the thermal velocity is defined as $v_t = \sqrt{\frac{k_b T_\perp}{m_a}}$. Here, we associate the random particle motion transverse to the propagation direction by a temperature $T_\perp$. The relationship in Eq. 3 is plotted in Fig. 4, which shows competing with the spot size of a 1 m ^{2} aperture laser ($\Omega = 10^{-12}$) requires a particle beam with MeV particle energy and micro-Kelvin temperatures, *simultaneously*. This illustrates that the large divergence of quasi-neutral plasma beams, such as proposed by Winglee [40], is the result of high plasma temperature [iv].

Unlike laser light, the area-divergence product of a particle beam can be reduced by the action of non-conservative forces, providing a means of extracting entropy (i.e. reduce random motion) from the beam. Indeed, decreasing Π by many orders of magnitude has already been demonstrated in the laboratory using a variety of laser-cooling approaches and geometries [41, 42, 43, 44, 45, 29]. Indeed, Nordley first proposed using laser cooling to reduce the transverse temperature of a sodium atom beam propulsion concept [37]. Laser-cooled particle beams are currently under development for high precision nanofabrication and surface modification with focused ion beams [29]. Additional details on the modern day application of laser cooling to laboratory atomic beams is described in Sec. 5.

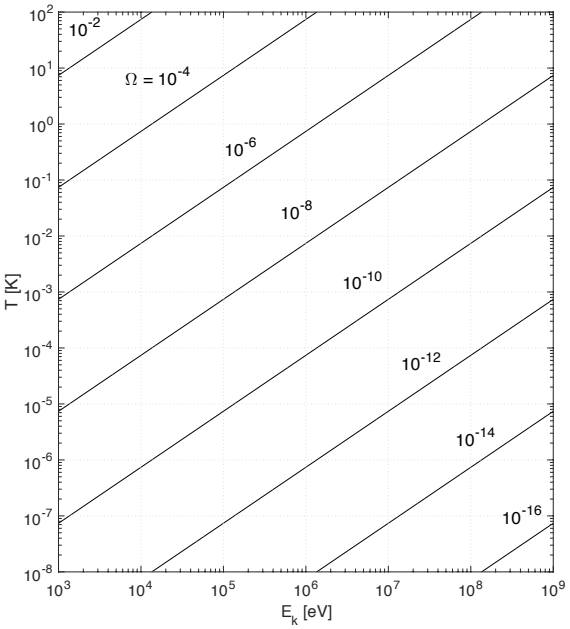

Figure 4: Divergence solid angle from Eq. 3, in steradians.

Here, we wish to highlight limitations on Π encountered by laser cooling approaches. Two physical limits are applicable to common laser cooling methods: the Doppler limit and the recoil limit. In a Doppler cooling scheme, the minimum achievable temperature is the Doppler temperature, which is dictated by the competition of Doppler cooling and re-emission processes [41]:

$$T_d = \frac{\hbar \Gamma}{2k_b}, \tag{4}$$

where $\hbar$ is the reduced Planck constant and Γ is the decay rate of the relevant optical transition [41, 42, 43, 44, 45, 46]. In a second cooling scheme, known as polarization gradient cooling, the minimum temperature is often near the limit imposed by the photon momentum recoil, known as the recoil temperature:

$$T_r = \hbar^2 k^2 / m_a k_b, \tag{5}$$

where $k = 2\pi/\lambda$ is the propagation constant of the cooling laser [46, 41, 47]. Table 1 gives relevant atomic data and Doppler and recoil temperatures for hydrogen and the alkali metal elements. Considering again Fig. 4, laser cooling the particle beam divergence enables values of Ω comparable to laser approaches.

[iv] Unneutralized on beams further expand due to Coulomb repulsion.

Table 1: Laser cooling parameters for the alkali elements.

Element	m_a [amu]	λ (D1) [nm]	$1/\Gamma$ [ns]	T_d [mK]	T_r [μK]
H	1	121.567	2.13	1.79	1296
Li	7	670.977	27.1	0.14	6.08
Na	23	589.756	16.3	0.23	2.39
K	40	770.108	26.7	0.14	0.79
Rb	87	794.978	27.8	0.14	0.36
Cs	133	894.593	34.9	0.11	0.18

In summary, geometric considerations show that laser and particle beam propulsion concepts are subject to similar system-level challenges with improving transmitter apertures and capture areas [v]. While laser technology currently exhibits superior values of Π, significant potential remains to be realized in particle beam systems. Matching the area-divergence product of lasers, $\Pi \sim 10^{-12}$, is possible, *in principle*, by applying laser cooling to high energy neutral beams. The only such attempt was reported by Lam and co-workers (1987), who investigated divergence reduction of hydrogen beams for space-based weapons systems [48] [vi]. Moreover, in addition to Π, the superior thrust-to-power ratio of particle beams has not been taken into account and is addressed in the following section.

In the context of the discussion above, *the objective of the proposed self-guiding beam is to disrupt the fundamental limitation embodied in Eq. 1 by using the laser and particle beams to continually refocus each-other during propagation, thereby overcoming the inherent limitation on L imposed by free-space propagation*. Notably, the interactions that give rise to self-guiding behave as linear optical elements, and thus do not change the value of Π for either the laser or particle beam separately. Consequently the beam entropy, associated with the phase-space volume of the beam [34], is preserved but not reduced during self-guided propagation.

1.3 Beamed Propulsion Dynamics

While Eq. 1 sets a characteristic focusing and acceleration distance for beamed propulsion, it is only one aspect of the propulsion dynamics. In this section, we summarize and compare the equations of motion of a spacecraft accelerating under the action of laser and particle beams. Through a comparison, we show the conditions under which laser and particle beam systems will provide similar payload capability. Notably, self-guided propulsion contains elements of both laser and particle thrust.

As illustrated in Fig. 1, while photons provide the highest specific impulse of any propulsion system, they also possess the lowest thrust-to-power ratio. In the non-relativistic limit, the thrust provided by a laser of power P_L incident on a surface of reflectance R_L and absorptance

[v] An ultimate limit on beam divergence arises from the Heisenberg uncertainty principle, which is equivalent to replacing λ in Eq. 1 by the deBroglie wavelength $\lambda_{dB} = h/\sqrt{2m_a E_k}$, where h is Planck's constant and E_k is the particle energy. This result can be derived, within a small multiplicative factor, from the position-momentum uncertainty relation applied to the beam aperture and transverse momentum. For a 1 MeV sodium beam, this limit is $\Pi = 3.4\times10^{-29}$ m^2, far less than practically achievable at the present time.

[vi] Such systems, presumably classified, are likely under continued development as indicated by recent budgetary requests: https://www.defenseone.com/technology/2019/03/pentagon-wants-test-space-based-weapon-2023/155581/

$(1 - R_L)$ is $T = (1 + R_L)P_L/c$. The relativistic correction is given by [4],

$$T_L = \frac{P_L}{c}(1 - \beta)\left(1 - R_L + \frac{2R_L}{1+\beta}\right) \tag{6}$$

where $\beta = v_{sc}/c$ [vii]. The thrust-to-power ratio is therefore near a constant value of $(1 + R_L)/c$ over most of the acceleration phase, declining somewhat as the velocity approaches c.

For particles, the beam power is given by the kinetic energy flow-rate,

$$P_p = \frac{1}{2}\dot{m}v_b^2 \tag{7}$$

where $\dot{m}$ is the flow-rate of mass through the beam source. The thrust imparted to a spacecraft depends on whether the particles are absorbed or reflected, the fraction of particles which are intercepted, and the relative velocity of the spacecraft and beam. In particular, the relative motion reduces the mass flow rate onto the spacecraft by a factor $(v_b - v_{sc})/v_b$ relative to that passing through the source. The thrust is then,

$$T_p = (1 + R_p)\dot{m}\frac{(v_b - v_{sc})^2}{v_b} \tag{8}$$

which in terms of the particle beam power is,

$$T_p = \frac{2(1+R_p)P_p}{v_b}\left(1 - \frac{v_{sc}}{v_b}\right)^2. \tag{9}$$

The thrust-to-power ratio goes to zero as the spacecraft approaches the beam velocity, and for $v_b >> v_{sc}$ peaks at $2(1 + R_p)/v_b$, which is greater than photon propulsion by a factor of $\sim 2c/v_b$. The latter suggests that the advantage of the particle beam is greatest for low velocity missions, although a $20\times$ improvement is still observed for $v_b = 0.1c$.

For the self-guided beam, the total thrust is a linear combination of Eq. 6 and Eq. 9, and the resulting dynamics, in the Newtonian limit, follow,

$$m_{sc}\frac{dv_{sc}}{dt} = T_L + T_p. \tag{10}$$

We defer a full relativistic treatment of the equations of motion to subsequent work, but note only that the relativistic correction to the particle beam and spacecraft masses are only 2% at a velocity of $0.2c$. In the Sec. 3, mission analyses are performed by integrating Eq. 10 (using Eq. 9 and Eq. 6) numerically, as no closed-form solution exists in the general case.

Finally, we consider the relative capability of laser and particle beam systems characterized only by their available power and Π. In particular, we aim to determine the key parameters that affect payload mass. Considering the case where $v_b >> v_{sc}$, and neglecting the relativistic

[vii] In the limit $\beta \to 0$ this reduces to the classical result.

correction to the laser thrust, constant acceleration motion is obtained in both cases. The final velocity after a distance L, given by Eq. 1, is then,

$$\frac{1}{2} m_{sc,L} v_{f,L}^2 = (1 + R_L) \frac{P_L}{c} \sqrt{\frac{A_t A_{sc}}{\Pi_L}}, \tag{11}$$

$$\frac{1}{2} m_{sc,p} v_{f,b}^2 = 2(1 + R_p) \frac{P_p}{v_b} \sqrt{\frac{A_t A_{sc}}{\Pi_p}}. \tag{12}$$

Each term in Eq. 12 represents a different aspect of the system design, such as the mission specification (final velocity), space infrastructure (power and transmitter area), and spacecraft subsystem (size and beam-spacecraft interaction). Comparing the beam systems for a similar mission ($v_{f,L} = v_{f,p}$) and power availability ($P_L = P_p$), the probe mass ratio is then determined by a small number of parameters. We can simplify the expression by considering a particle beam with an area-divergence product given by $A_t \pi (v_t / v_b)^2$, which results in,

$$\frac{m_{sc,L}}{m_{sc,b}} = \frac{1+R_L}{4(1+R_b)} \frac{v_t}{c} \frac{D}{\lambda}, \tag{13}$$

where D is the transmitter diameter.

While many assumptions and simplifications have gone into Eq. 13, it serves to highlight the most important drivers of system design in particle and laser beamed propulsion. Namely, the key parameter maximizing laser payload is the diffraction angle, while for particle beams it is minimizing the transverse thermal velocity. For a thermal particle source, v_t may be of order 300 m/s, in which case $c/v_t = 10^6$. Comparing this with a 1 μm wavelength and 1 meter diameter aperture laser system, where $D/\lambda = 10^6$, we would expect similar overall performance.

Eq. 13 may prove useful when considering future technology improvements. For example, new on-orbit construction or laser cooling technologies may permit 200 meter diameter optical apertures and particle beams with a transverse velocity of $v_t = 0.29$ m/s (at the Doppler temperature of ^{23}Na, 0.14 mK). In this scenario, $m_{sc,L}/m_{sc,b} = 0.096$ and the particle beam payload is a factor of 10 larger than the laser beam payload. Clearly, different assumptions regarding technological challenges and economic cost of improved laser and particle beam systems will determine the outcome of estimates by Eq. 13 and the above example is only meant to demonstrate its utility.

In summary, Sec. 1 has introduced the self-guided beam concept and placed it in the context of conventional beamed propulsion using laser and particle beams. We reiterate a critical distinction, that **the self-guided mode of propulsion is not constrained by Eq. 1**, and can in principle exceed the characteristic distance L by an unknown amount. The sections which follow describe the physics of the self-guided beam, the conditions under which self-guiding can occur, mechanisms that may disrupt self-guiding, and ultimately the estimated payload performance for interstellar missions.

2 Self-Guided Beam Physics

In this section, we present the historical context and governing equations of the self-guided beam propulsion concept. In particular, we aim to provide a foundational theoretical basis of the underlying physics and relevant light-matter processes for future analysis of the beam system.

2.1 Literature Review

The mechanism of self-guiding through vacuum is the combination of a waveguide effect due to the particle refractive index, and an optical force, known as the *optical dipole force*, that draws particles into the intensity maxima. The above photon-particle coupling was first studied by Askar'yan in 1962 as a mechanism for optical self-guiding and the holding off of gases against vacuum [15]. After the milestone experimental demonstration of laser guiding (trapping) of particles using the dipole force by Ashkin and co-workers in 1978 [49], Klimontovich was the first to note a corresponding light guiding effect should be observed in Ashkin's experiments [16]. Thus the basic physical principles and conception of self-guiding, utilizing density-driven changes in the refractive index and the dipole force, was in place as early as 1979.

In their recent review on opto-mechanically coupled beams, Saffman and Skryabin noted that few authors treat the governing equations for the light and atomic beams self-consistently, as in most experiments one or the other is dominant [50]. In the past two decades, several groups have developed fully quantum models for the self-guided light and matter propagation consisting of Bose-Einstein condensates (matter waves) and lasers [17]. Attempts to observe self-guiding in ultra-cold, degenerate gases have also been made [51]. Several research efforts have focused on understanding self-structuring, or pattern formation, in cold atomic gases with recirculating [19, 18] or back-reflected laser beams, the effects of which have now been experimentally observed [20]. Each of these studies exploits the same fundamental interactions we invoke here for self-guiding and highlight that the underlying physical principles, exploited here for propulsion, are currently observed and investigated in other related contexts.

2.2 Physical Basis for Self-Guiding

In the following, we present a detailed classical picture of the self-guided beam physics, which emerges from the coupled interaction between classically interacting optical fields and particles. In what follows, we consider an idealized system consisting of axisymmetric (cylindrical) particle and laser beams propagating together in the z-direction, as shown in Fig. 5. The particle beam is characterized by its density $N(\mathbf{r})$, atomic mass m_a, the velocity aligned with the z-axis, v_b, and transverse and longitudinal temperatures, $T_\perp$ and $T_{||}$ respectively. The laser beam, which is overlapped with the particle beam, is defined by its wavelength λ in the transmitter reference frame, and intensity $I_L(\mathbf{r}) = \frac{1}{2Z_0}|\mathbf{E}(\mathbf{r})|^2$, where $Z_0 = \epsilon_0 c = 377\ \Omega$ is the impedance of free space and $\mathbf{E}$ is the electric field. Each of these two beams has its own respective cross-sectional area, A_p for the particle beam and A_L for the laser beam, which in general may be different.

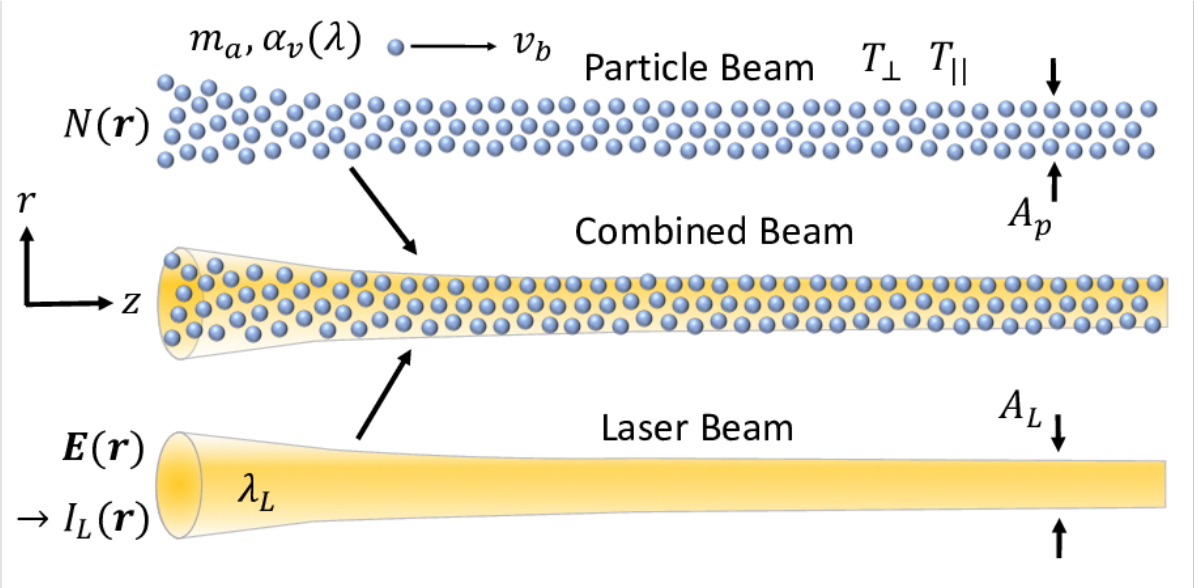

Figure 5: Physical parameter breakout of the laser and particle beams.

2.2.1 Light Guiding Mechanism

Both the light guiding and particle trapping effects arise from the linear electric polarizability of matter. That is, an electric field applied to an atom induces a dipole moment $\mathbf{d}$,

$$\mathbf{d} = 4\pi\epsilon_0\alpha_v\mathbf{E} \tag{14}$$

where ϵ_0 is the permittivity of free space and α_v is the volume polarizability of the atom. The polarizability of matter gives rise to the dielectric constant ϵ and refractive index η of media and has been known since the early experiments by Tyndall to provide a light guiding effect in fluids. The refractive index of a dilute gas is directly proportional to its density:

$$\eta(\mathbf{r}) = 1 + 2\pi N(\mathbf{r})\alpha_v(\lambda). \tag{15}$$

For a positive polarizability the refractive index is larger at the particle beam center where the density is highest. Indeed, light guiding requires spatial variations in the refractive index, which can take the form of discrete changes, such as in common step-index optical fibers, or continuous gradations. While guiding in multi-mode and graded index fibers can be explained by ray tracing or through the effect of total internal reflection [52], the governing equations of beam propagation require a more rigorous approach including diffraction.

For large beams, laser propagation can be modeled by the paraxial wave equation, which is derived from Maxwell's Equations in media (see Appendix 8), provided the beam is harmonic, dilute and weakly guided [52]:

$$2ik_0\frac{\partial E}{\partial z} = \nabla_\perp^2 E + k_0^2(\eta^2 - 1)E. \tag{16}$$

Here, E is the scalar amplitude of the electric field (a complex function), $k_0 = 2\pi/\lambda$ is the propagation constant, $\nabla_\perp^2$ is the part of the Laplacian perpendicular to z, and β is the propagation constant. The particle beam acts as a waveguide whose guided modes satisfy $\partial E/\partial z = 0$, which forms the basis of the theory of waveguides with weak guiding [52].

The number of guided modes and their characteristics are known to depend on the V-parameter, *which describes the relative strength of guiding and diffraction*. For dilute gases in vacuum [52],

$$V^2 = 8\pi \frac{A_p \delta\eta}{\lambda^2} \tag{17}$$

where $\delta\eta = \eta - 1$ is the refractive index contrast. Strong light guiding requires confinement of the laser power primarily within the waveguide structure (the particle beam in this case), corresponding to $V \sim 2$. This approach is consistent with the literature on Kerr effect self-guiding and laser filamentation, where self-focusing emerges from an intensity non-linearity of the refractive index [53, 54]. Derivations of the critical power for self-focusing equate the diffraction angle of a beam with the angle of total internal reflection, resulting in a condition on the refractive index contrast given by [53],

$$\delta\eta = K\lambda^2/A_p, \tag{18}$$

where K is a constant which varies from 0.14 - 0.16 depending on the beam intensity profile [54]. We observe that $V = 2$ corresponds to $K = 1/2\pi = 0.159$, consistent with the literature on filamentation. Combining Eqs. 18 and 15, the guiding condition can be expressed in terms of the beam density, atomic polarizability, wavelength and particle beam area:

$$A_p N(0) = \frac{V^2}{8\pi^2} \frac{\lambda^2}{\alpha_v(\lambda)}, \tag{19}$$

where $N(0)$ signifies the density on axis [viii]. Thus, the light guiding condition equations the linear density of particles (left-hand side of Eq. 19) with a ratio of the diffraction effect ($\lambda^2 = \Pi$ for the laser) and the dipole polarizability.

Notably, the right-hand side of Eq. 19 depends only on wavelength, as indicated by the explicit dependence of α_v on λ. Calculation of the wave-dependent polarizability is obtained from the semi-classical Sellmeier equation [55],

$$\alpha_v(\lambda) = 0.0702 \text{ nm}^3 \sum_j \frac{f_{0j}}{1/\lambda_{0j}^2 - 1/\lambda^2}, \tag{20}$$

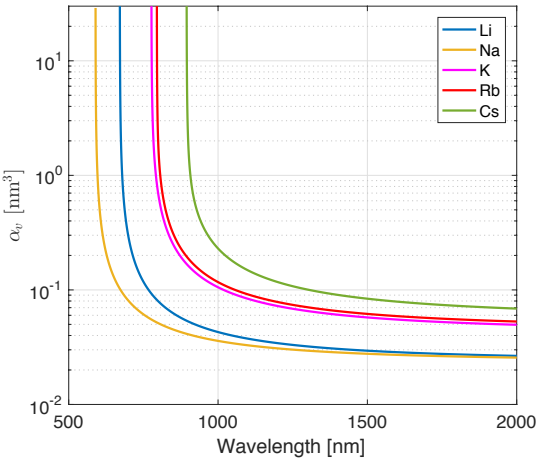

Figure 6: Wavelength-dependent polarizability of the alkali atoms.

where f_{0j} are the transition oscillator strengths from the ground state and λ_{0j} are the wavelength

[viii] Note that for a moving beam the value of α_v must be taken at a Doppler shifted wavelength $\lambda' = \lambda(1 - v_b/c)$.

of the transitions in microns [ix]. Calculations for the alkali elements are shown in Fig. 6, which demonstrate the significant enhancement near the D1 transitions which can reduce the necessary linear particle density imposed by Eq. 19.

The above discussion shows that the light-guiding phenomena arises from density variations in the particle beam, and that the effect may be enhanced near atomic resonances. In the following sections, Eq. 19 and 20 will be used for low-fidelity mission design, while Eq. 20, 16 and 15 are applied toward high fidelity modeling of the beam propagation.

2.2.2 The Dipole Force and Stochastic Heating

In the previous section, regions of high refractive index, and thus density, were shown to enable a light-guiding effect. In this section, we describe the corresponding effect of the laser beam acting to confine particles in regions of high intensity. Since the seminal experiments of Ashkin, [56, 57, 58], this process has been exploited in a wide range of applications, such as laser trapping of microparticles (optical tweezers) and atoms.

Although the trapping of atoms can be treated through classical electrodynamics, the dipole force on single atoms is best understood through the semi-classical quantum treatment of the two-level atom [41, 46, 55]. By considering a two-level atom interacting with a time harmonic, classical electromagnetic field, the force on an atom is found to consist of two parts: one associated with absorption and scattering of radiation and a second associated with a Stark shift of the atomic ground state energy. The former, known as the scattering force, results in a time-averaged radiation pressure acting in the direction of beam propagation.

The second term, known as the optical dipole force or gradient force, acts in the direction of the beam intensity gradient and *is an essentially conservative force*. The neutral particles are confined to the laser beam by the dipole force, which can also be derived classically by applying the Lorentz force law to the individual bound charges of the quasi-neutral atom or, alternatively, an idealized point electric dipole [59]. While there is a slight difference in the formal result of each approach (giving rise to the so-called Abraham-Minkowski controversy [60]), the optical force F averaged over an optical period is:

$$\mathbf{F} = -\frac{2\pi}{c}\alpha_v \nabla I_L(r). \tag{21}$$

In Eq. 21, if α_v is positive, corresponding to an increased refractive index and light guiding, the atoms are drawn towards the intensity maximum, resulting in confinement of the particle beam. The dipole force may also be associated with an energy potential (the "optical dipole potential") [46],

$$U = -\frac{2\pi}{c}\alpha_v I_L. \tag{22}$$

The optical dipole potential has been used extensively in the trapping and manipulation of cold atoms, and a thorough review can be found in Grimm (1999) [46]. Provided that the sum of the kinetic and potential energy are less than zero, a particle will remain confined within the laser

[ix] For the alkali elements, calculations by Eq. 20 using only the D1 and D2 transitions yield accurate results provided the transitions are not saturated.

beam while simultaneously providing the guiding effect. The strength of the trapping force can be increased either through I_L or $\alpha_v(\lambda)$, the latter of which can be enhanced near atomic resonances, as seen in Fig. 6.

It would be natural to try and enhance trapping forces by tuning very close to atomic resonances, where α_v increases dramatically. However, increasing α_v can be detrimental to the trapping lifetime. Indeed, when the first dipole traps were constructed, investigators tuned very close to the D-line resonances of alkali vapors in order to increase the trapping force [49]. However, it was observed that confinement times were severely limited by a heating effect associated with the spontaneous, randomly-directed scattering of photons. Over many scattering events, the trapped atoms undergo a random walk in momentum space due to randomly-directed photon recoils, leading to a linear heating rate given by $k_b T_r R_{sc}$, where R_{sc} is the scattering rate.

Near resonances, R_{sc} approaches a maximum of $\Gamma/2$ under saturated conditions [41], which can be larger than 10^7 Hz (see Table 1). Under these conditions, the atoms will be heated to 10 million times the recoil temperature in one second and likely escape the trap far earlier still. Fortunately, the scattering rate drops of as $1/\Delta^2$ while the trapping force decreases as $1/\Delta$, where Δ is the frequency detuning from resonance. Thus, far off-resonance the scattering rate can be virtually eliminated while maintaining a sufficiently deep dipole potential [46]. The development of these types of traps, such as the far-off-resonance trap [61] and quasi-electrostatic trap [62], have enabled atom trapping over many minutes to study coherent phenomena of atomic ensembles. In this regime, R_{sc} can be considered as Rayleigh scattering, rather than resonance fluorescence, which gives a scattering rate,

$$R_{sc} = \frac{\sigma_R I_L}{\hbar\omega}, \tag{23}$$

where the Rayleigh cross section is [55, 63],

$$\sigma_R = \frac{8\pi}{3} k^4 |\alpha_v|^2. \tag{24}$$

From the preceding discussion, we identify an important trade-off, namely, while increasing the polarizability deepens the dipole potential linearly with α_v, the scattering rate (and thus heating rate) increases quadratically. Furthermore, both the scattering rate and dipole force scale linearly with laser intensity. As discussed by Grimm and co-workers [46], an expression for the trap lifetime can thus be derived based on the dipole potential depth and heating rate in a 2D trap. Approximating the trap potential as a harmonic well, the Virial theorem is used to arrive the following energy equation [46]:

$$\frac{dT}{dt} = \frac{2}{5} T_r R_{sc}. \tag{25}$$

The solution to Eq. 25 is linear in time, and after substitution by Eq. 5, Eq. 59 and Eq. 24, the time to raise the kinetic energy of the particle ensemble by an amount equal to the trap potential depth is [x],

[x] Here we have invoked the fact that far off-resonance the polarizability is primarily real and thus $Re(\alpha) \rightarrow |\alpha|$ [55].

$$t_h = \frac{5m_a\lambda^5}{128\pi^5\hbar\alpha_v}, \tag{26}$$

Notably, Eq. 26 only depends on the atomic species and wavelength, and demonstrates that minimizing the polarizability-to-mass ratio $\alpha_v(\lambda)/m_a$ will result in the maximum confinement time at a given wavelength. [xi] As shown in Fig. 7(left), the heating time becomes very short near the alkali resonances. The fundamental trade-off between trapping strength and heating is embodied in Fig. 7(right), demonstrating that heating time and polarizability must be traded against on-another in choosing the parameters of the self-guided beam.

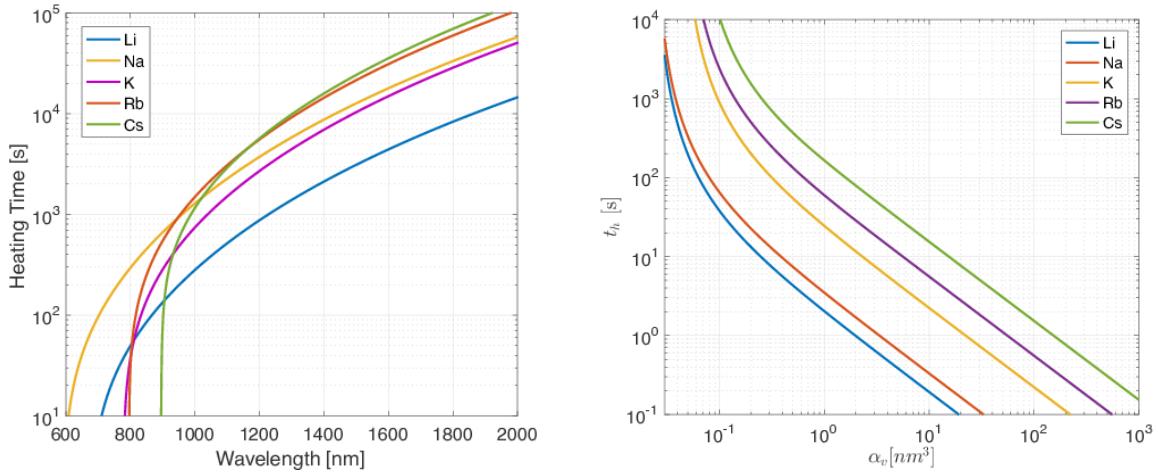

Figure 7: Heating time t_h as a function of wavelength (left) and polarizability (right).

2.2.3 Particle Dynamics

Having described the relevant optical forces in the previous section, we now shift focus to particle motion, which follows the first-principle gas kinetic equation subject to applicable forces. The individual particles will evolve subject to Newton's laws of motion:

$$m_a \frac{d\mathbf{v}}{dt} = \mathbf{F} \tag{27}$$

$$\frac{d\mathbf{v}}{dt} = \mathbf{v}. \tag{28}$$

For an ensemble of particles, the evolution of the phase-space distribution function f is given by the Boltzmann equation,

$$\frac{\partial f}{\partial t} + \mathbf{v}\cdot\frac{\partial f}{\partial r} + \frac{\mathbf{F}}{m_a}\cdot\frac{\partial f}{\partial \mathbf{v}} = S, \tag{29}$$

where f is a function of particle position r, particle velocity v, and time t. Additionally, F is the total optical force exerted on particles, and S is the collision term. The number density of the

[xi] Equation 26 should be considered a lower bound because particles in a Gaussian potential well will spend more time in low intensity regions as compared to a quadratic well, leading to longer confinement times. For example, in a $1/r$ trapping potential Eq. 25 the heating rate decreases exponentially with increasing temperature. We can also surmise that if the scattering rate is less than the "orbital" period, escaping particles will exhibit velocities consistent with the *recoil temperature* at the trap wavelength, which are significantly below the Doppler temperature.

particles can be calculated from the moment of the VDF: $N(\mathbf{r}) = \int f(\mathbf{v})d\mathbf{v}$, which affects the laser propagation via Eq. 15 and Eq. 16.

2.2.4 Trapped Fraction

In this section, we analyze the initial overlap of the laser and particle beams and apply the trapping condition to a particle distribution function f. This analysis allows us to 1) relate the trapping potential depth U to the temperature of the gas particle $T_\perp$, and 2) relate the laser beam area A_L to the particle beam area A_p. Both of these relationships will be important later in constructing a credible framework for beam parameter optimization in Sec. 3.

We begin by considering a particle, injected into the dipole potential at some initial location, which evolves subject to Newton's laws of motion. It remains confined only if sum of its kinetic and potential energy are less than zero. To achieve the requisite light-guiding effect at a particular wavelength (Eq. 19), a sufficient number of atoms must be trapped. Essentially, the thermal energy of the atomic beam must be substantially less than the trapping potential depth [xii]:

$$k_b T_\perp \leq |U(0)|. \tag{30}$$

In order to develop a more exact relationship between the trap depth and temperature, we consider the initial overlap phase of laser and particle beams of variable width and proceed to calculate the fraction of trapped particles as a function of the initial gas temperature and potential depth. We assume an initially Gaussian distribution of the laser intensity, dipole potential, and particle density:

$$I(\mathbf{r}) = I_L \ \exp(-2r^2/w_L^2) \tag{31}$$
$$U(\mathbf{r}) = -U(0)\exp(-2r^2/w_L^2) \tag{32}$$

where w_L is the $1/e^2$ width of the laser beam, following the convention for Gaussian beams, and,

$$N(\mathbf{r}) = N(0) \ \exp(-r^2/r_n^2), \tag{33}$$

where r_n is the $1/e$ width of the particle beam. A particle injected at some location r in a laser beam will remain trapped provided its kinetic energy is less than or equal to $|U(\mathbf{r})|$. For an ensemble of particles with an initially Maxwellian velocity distribution, the cutoff corresponds to a circle in the v_x, v_y plane of radius $v_\perp = \sqrt{v_x^2 + v_y^2} = \sqrt{2|U(\mathbf{r})|/m_a}$, and the fraction of trapped particles is obtained by integrating over the 2D velocity distribution function:

$$f(v_\perp)dv_\perp = \frac{m_a}{2\ k_b T_\perp}\exp(-m_a v_\perp^2/2k_b T_\perp). \tag{34}$$

Integrating from 0 to $v_{max} = \sqrt{2|U(\mathbf{r})|/m_a}$, we obtain the fraction of particles F_{trap} at initial location r which are trapped:

[xii] In practice, the trapped atomic gas is never in thermal equilibrium, since any atoms in the tail of a Maxwellian distribution will have sufficient energy to escape the trap. Rather, the factor $k_b T_\perp$ is more correctly associated with the velocity distribution function.

$$F_{trap}(\mathbf{r}) = 1 - \exp(-|U(\mathbf{r})|/k_b T_\perp). \quad (35)$$

As seen in Eq. 35, the fraction of trapped particles at any location r only depends on the ratio $|U(\mathbf{r})|/k_b T_\perp$.

We now proceed to calculate the total fraction of trapped particles over the entire particle beam and the dependence on the beam widths, defined by Eq. 33 and Eq. 32. The net fraction of trapped particles is found by taking a weighted average of F_{trap} over the entire beam:

$$F_{net} = \frac{\int_0^\infty 2\pi r N(r) F_{trap}(r) dr}{\int_0^\infty 2\pi r N(r) dr}. \quad (36)$$

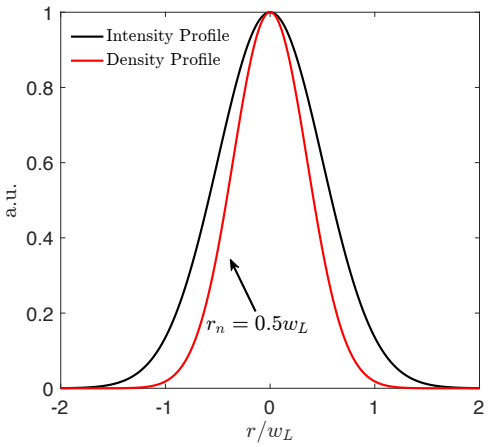

Figure 9: Intensity and density profiles. consistent with

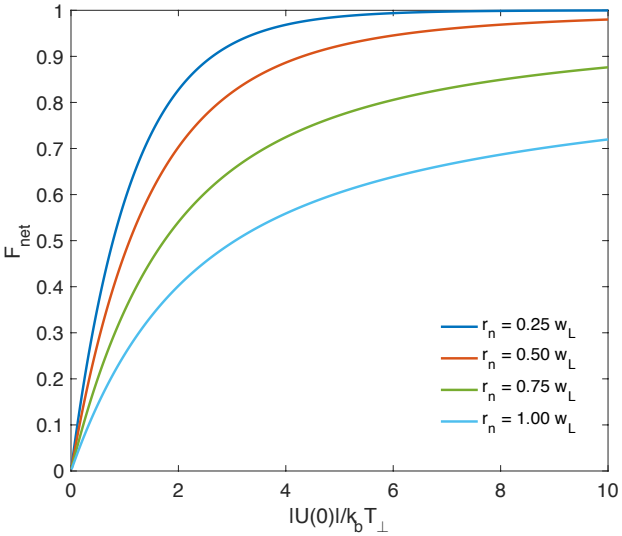

Figure 8: Dependence of the trapped fraction on the trapping potential depth with different initial particle beam sizes.

The dependence of F_{net} on both $|U(0)|$ and r_n can be seen in Fig. 8, which illustrates that as the ratio r_n/w_L increases, the fraction of trapped particles decreases since more atoms start at a higher potential energy. We observe that nearly 90% of the atoms are initially trapped for the conditions $r_n = 0.5w_L$ and $|U(0)|/k_b T_\perp = 4$. The corresponding spatial profiles of density and laser intensity ($r_n = 0.5w_L$) are shown in Fig. 9. The above conditions are used in subsequent mission designs to relate the laser beam area and potential depth to the particle beam area and temperature, respectively.

2.3 Loss Processes and Destruction of Self-Guiding

The physical mechanisms described in the previous section permit self-guided solutions, as already found in analogous quantum degenerate systems [50]. However, the dynamic stability of the self-guided beam is currently an active area of study [19].

In the context of propulsion, the problem is multi-fold: 1) if self-guiding solutions to the governing equations exist, how might one produce them in a practical system? 2) What are the consequent constraints on the beam system? 3) If a self-guided beam can be produced, by what mechanism is it destroyed? 4) How is the beam stability affected by relevant non-dimensional parameters? And finally, 5) if the beam is unstable, can dissipative mechanisms, such as particle heating or low-speed collisions, or second-order effects, such as laser beam polarization or Kerr effect, be tuned to restore stability? Quantitative answers to these questions are beyond the scope

of this report, and require a stability analysis of the governing equations in concert with high fidelity numerical simulation of the fully coupled system. In the following sections, we seek only to enumerate and analyze the key physical mechanisms which affect beam parameters during propagation.

Below, we examine several light-matter interactions that affect the light guiding and particle trapping conditions, including 1) Rayleigh scattering, 2) collisions, and 3) multi-photon ionization. In addition, the particle heating effect described in Sec. 2.2.3 depletes the particle beam through particle escape. These processes can deplete the laser and particle beam elements, reducing the important non-dimensional parameters for guiding: $|U(0)|/k_b T_\perp$ and V.

The overall effect of these variations on beam stability is unknown, as the guiding conditions are not hard equalities. That is, a small reduction of the V-parameter or a small reduction in the trap potential depth will not necessarily result in destruction of self-guiding. On the other hand, we cannot reasonably expect endless self-guided propagation. Eventually the key beam parameters, for example the mass flow rate or particle or laser beam spatial profiles, will be "significantly" disturbed from their initial values, resulting in a dynamic loss of self-guiding. While the degree of stability or instability cannot be addressed at this time, we present below an assessment of the physical phenomena that result in losses of particles or photons and may disrupt self-guiding. In this analysis, we identify important trade-offs but no "show-stoppers". In addition to light-matter interactions, we assess the effects of gravity and transmitter location and show that guiding of light around a gradual bend does not impose onerous restrictions on the beam system.

2.3.1 Rayleigh Scattering

While light scattering gives rise to particle heating, as described in Sec. 2.2.3, it also results in attenuation of the optical beam and therefore reduction of the trapping potential depth (Eq. 22). In this subsection, we consider laser attenuation due to scattering loses and proceed to find the characteristic distance over which this occurs.

Far-off resonance, attenuation from light scattering and the classical "absorption" coefficient (described by an imaginary part of the refractive index) are one and the same, a consequence of the Optical Theorem [55]. Attenuation is thus described by the Beer-Lambert law, with an "absorption" coefficient reflecting attenuation by Rayleigh scattering,

$$\frac{dI_L}{dz} = -\alpha_{rs} I_L \tag{37}$$

where the attenuation length is given by,

$$\alpha_{rs} = N\sigma_R(\lambda), \tag{38}$$

and the Rayleigh cross section is given by Eq. 23. The characteristic length over which the light attenuates is thus $1/\alpha_{rs}$. Using the Sellmeier equation (Eq. 20), scaling of the attenuation length

has been calculated for a density of 10^7 cm^{-3} and 10^9 cm^{-3}, as shown in Fig. 10.

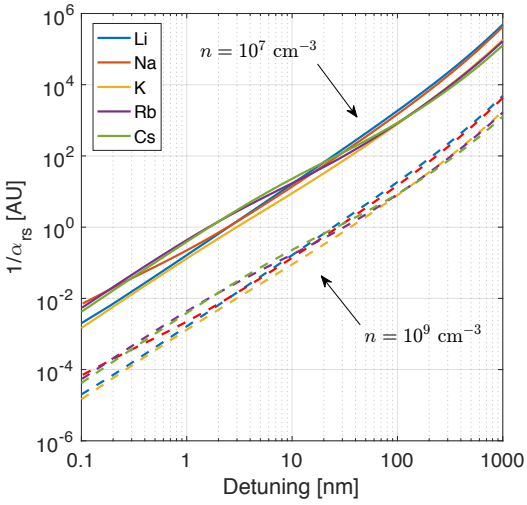

Figure 10: Characteristic attenuation distance due to Rayleigh scattering, as a function of detuning from D1 resonance.

Over the entire range, the attenuation length increases approximately quadratically with detuning, dominated by the near-resonant enhancement of the polarizability. Depending on the particle density, and the detuning needed to achieve the trapping and light guiding requirements, the attenuation length can become prohibitively short. Detuning of at least several nanometers is needed for AU propagation distances. In practice, we have found that the heating effect (Sec. 2.2.3) imposes a much stricter requirement on beam propagation. This occurs because for equal photon and laser beam power, the photon-to-particle ratio is $E_k/\hbar\omega$ which is of order 50 MeV / 1 eV = 5×10^7. Since only order $\sim$ 1000 scattering events are needed to heat the particles by 1 mK, only a small fraction of the beam is attenuated by the time most particles escape the potential well.

2.3.2 Collisions

Particle collisions may be detrimental to self-guided propagation, as scattering out of the self-guided beam reduces the beam density, V-parameter, and therefore guiding ability (see Sec. 2.2.1). Two distinct types of collisions can be identified: those between a beam particle and a solar wind particle and those between two beam particles.

In the former case, the relative velocities are so high that any collision will result in particle loss. The attenuation length of the particle beam by the solar wind can be calculated from the neutral-ion collision cross-sections for the beam atoms with protons, which dominate the solar wind [64]. Choosing the appropriate cross section is complicated by the importance of very slight grazing collisions. These collisions occur at a large impact parameter and are mediated by the interaction between the proton and atomic dipole induced by the Coulomb field. While stronger than the van der Waals interaction between neutral atoms or molecules, the interaction is weaker than ion-ion scattering. Thus, the resulting cross section is much lower than that predicted by the Rutherford formula which is often used for large deflection angles [xiii]. For estimates, we use a proton-neutral cross-section of $\sigma_{pn} \sim 1$ nm^2.

At a distance of 1 AU, the average solar wind proton density during the first half of 1990 was measured by the ACE spacecraft as $n_0 = 7.0$ cm^{-3} at a temperature of 10^5 Kelvin [64]. For most missions, the beam system will be pointing away from the sun, where the solar wind density decreases with distance. With these parameters, the mean free path is given by $\lambda_{mfp} =$

[xiii] Large deflection angles correspond to small impact parameter parameters near the unshielded atomic nucleus.

$1/n_0\sigma_{pn}$, which results in $\lambda_{mfp} = 0.95$ AU. In a more rigorous analysis, the radial density of the solar wind can be approximated by a $1/r^2$ dependence (see [64], i.e. $n(r) = n_0/r^2$ where r is the distance from the sun, so that a radially directed beam will attenuate following,

$$\dot{m}(z) = \dot{m}_0 \ \mathrm{e}^{-\int_0^z n_0\sigma_{pn}(1+z\prime)^{-2}dz\prime}, \tag{39}$$

where $n_0 = 7$ cm $^{-3}$ is the particle density 1 AU and we consider a transmitter at 1 AU ($z = r - 1$ AU).

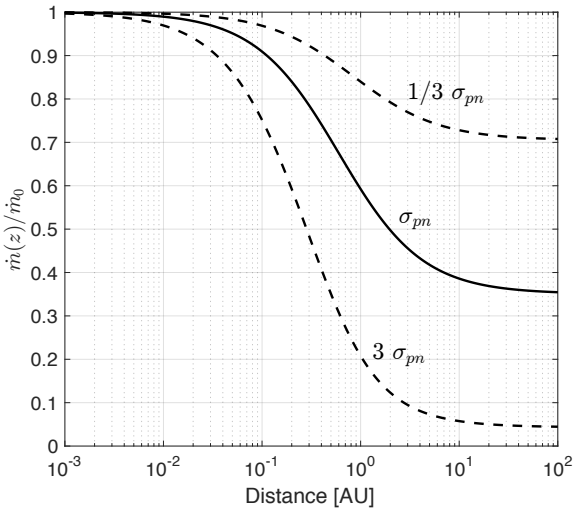

Figure 11: Attenuation of the particle beam with distance from transmitter.

Attenuation of the particle beam with distance is shown in Fig. 11, using the cross section of 1 nm ^{2} and variations by a factor of three. In each case, the beam attenuates until the solar wind density drops below a certain threshold, allowing the beam to escape into the more rarefied outer regions of the solar system. In all cases, negligible beam attenuation occurs over 0.01 AU and only a 30% decline in mass flow over 0.1 AU is observed for the largest cross section. However, Fig. 11 underscores the importance of determining an accurate cross section for the individual collision species (alkali metals) as part of future work.

Next, we consider collisions between the beam particles themselves. These collisions are important, as both collisions of the ensemble at $T_\perp$ or the thermalization of $T_\perp$ and $T_\parallel$ can result in post-collision energies larger than the dipole potential depth.

Unlike collisions with the solar wind, the characteristic distance between collisions, as viewed from an observer at rest, is not the mean free path but the product of the beam velocity and collision time τ_c. This distance we refer to as the collision interval d_c,

$$d_c = v_b\tau_c, \tag{40}$$

where the collision time is determined by the thermal velocity and mean-free-path of the beam atoms,

$$\tau_c = \frac{1}{N\sigma_{nn}v_t} \tag{41}$$

where v_t is the thermal velocity of the beam and σ_{nn} is the neutral-neutral collision cross section. The relevant thermal velocity is calculated from the larger of the transverse or longitudinal temperatures [xiv]. A first-principles calculation of beam temperature will require detailed modeling of source plasma, ion beam extraction, acceleration (ion optics) and neutralization. For estimates of τ_c, we take the hard-sphere cross-section $\sigma_{nn} = \pi d^2 \sim 1$ nm ^{2}, where d is the particle

[xiv] Here we see the importance of a highly monochromatic (monoenergetic) particle beam.

diameter. Considering a beam traveling at 0.01c with a thermal velocity of 100 m/s and density 10^{11} cm^{-3}, $\tau_c = 0.1$ s and $d_c = 3000$ km. While significant, this distance would place a severe constraint on beam propagation. If instead we consider a beam with a thermal velocity of 1 m/s and a density of 10^9 cm^{-3}, we find $\tau_c = 1000$ s and $d_c = 0.23$ AU. Considering mission parameters in Sec. 3, we find that stochastic heating competes with collisions as the primary limitation on propagation distance.

The above estimates demonstrate the relevance of collisions and the need for further investigations. The importance of collisions depends substantially on the beam parameters, such as the temperature, density and atomic mass of the atoms. Because light guiding is related to the linear particle density 19), the beam velocity, area and power directly influence the collision time as part of mission design (Sec. 3).

Finally, we note that the cross section used above could be an underestimate, since ultra-low temperature collisions are quantum-mechanical and exhibit a larger cross section [xv] [47, 65]. In this scenario, scattering of alkali atoms occurs primarily through the s-wave channel, and the cross section, *in the limit of zero temperature*, can be calculated from the characteristic scattering length a [47],

$$\sigma_{nn} = 8\pi a^2. \tag{42}$$

A table of scattering lengths for the alkali atoms can be found in Table 1 in Inguscio [66]. The values of a vary considerably depending on the atomic isotope and molecular potential energy curve (singlet or triplet), ranging from ~ 1.3 nm (triplet ^{7}Li) to ~ 160 nm (singlet ^{85}Rb). An intermediate value of of 4.5 nm results in a cross section $500\times$ larger than the 1 nm^2 estimate above. Some species also possess negative scattering lengths, which allow for a velocity range with zero scattering length and thus vanishing cross section [66]. For these species, collisions may potentially be suppressed almost entirely.

In summary, the dependence of cold-collision properties on individual atomic species and isotopes suggests that collisions may be one of several relevant criteria in the selection of the best atomic species, especially for laser-cooled neutral particle beams. Future investigations and detailed modeling will need to include cold-collision physics to accurately model cold atom beam sources.

2.3.3 Multi-Photon Ionization

Photo-ionization is a light-matter process resulting in loss of both photons and particles. The latter are lost because the ion and electron species no longer exhibit the dipole polarizability of the atom, α_v, and are unconfined to the trapping potential. The following section examines this potential loss mechanism.

The ionization energy U_i of the species under consideration range from 3.8 eV (Cs) to as much as 13.6 eV (H), with most alkali metals falling in the range 4 - 5 eV. Direct photo-ionization is thus energetically precluded, given infrared photons with energy ~ 1.17 eV ($\lambda = 1.06\,\mu$m). However, under intense illumination, atoms and molecules may be ionized through nonlinear

[xv] In essence, the deBroglie wavelengths of the particles are comparable or larger than the width of the molecular potential energy curves.

processes [67].

Depending on the laser field strength and frequency, three regimes can be identified: multi-photon ionization (MPI), tunnel ionization and over-the-barrier (OTB) ionization [54]. While the transition between tunnel and OTB ionization is determined by field strength alone, the transition from MPI to tunnel ionization is governed by the Keldysh parameter [54]:

$$\gamma = \frac{\omega\sqrt{2m_e U_i}}{e|\vec{E}|} = \sqrt{\frac{U_i I_c}{e I_L \lambda^2}} \tag{43}$$

where we have rewritten the formula conveniently in terms of the laser intensity, wavelength and the characteristic current $I_c = \epsilon_0 m_e c^3/4\pi^2 e = 34.36$ Amps [xvi]. In the limit $\gamma << 1$, ionization proceeds through tunnel ionization or OTB ionization, whereas $\gamma >> 1$ indicates a MPI mechanism. Even for a high intensity of 10 MW/cm^2, $\lambda = 1.06\mu$m and $U_i = 4$ eV, we find $\gamma = 111$, indicating that ionization rates calculated in the MPI limit will be valid. For the alkali metals Na, K, Rb and Cs, detailed calculations for three-photon MPI were performed by Bebb [68], while two and three-photon ionization rates for Li can be found in Chang and Polk [69]. The wavelength dependence exhibits resonances when the single or two-photon energy falls near an energy level accessible through the single or two-photon selection rules, respectively [67]. The characteristic time over which the neutral beam will be ionized by the laser can be determined from the MPI ionization rate w_i $[s^{-1}]$,

$$\tau_i = \frac{1}{w_i} \tag{44}$$

where the MPI rate is given by,

$$w_i = \sigma_{N_k}(\lambda)\left(\frac{I_L\lambda}{hc}\right)^{N_k} \tag{45}$$

where N_k is the number of photons required to ionize and σ_{N_k} is the MPI cross section [xvii]. As a typical off-resonant value for three-photon ionization of the alkali atoms, we find $\sigma_3 = 10^{-76}$ cm^6 s^2, which at an intensity of 1 MW/cm^2 yields $\tau_i = 113$ s. While this rate is very slow relative to typical MPI experiments with pulsed lasers, it is quite significant here. The heating time as a function of wavelength for cesium and lithium can be seen in Fig. 12, computed with the results from Bebb and Chang and Polk [68, 69]. Very short ionization times are observed seen near resonances and at high intensity, due to the nonlinear scaling with I_L^3.

At longer wavelengths (e.g. 1.06 μm), MPI proceeds through a four (Cs, Rb, K) or five (Na, Li) -photon process. In general, off-resonance and at fixed intensity, the MPI rate decreases as N_k increases. While four- and five-photon MPI rate calculations such as those of Bebb are not available in the literature, the four-photon cross-section of Cs at 1.056 μm was measured by Morellec and co-workers as $\sigma_4 = (8 \pm 3)\times 10^{-109}$ cm^8 s^3 [70]. For an intensity of 1 MW/cm^2, we find $\tau_i = 100.2$ years, which is negligible. The preceding estimates suggest that while photoionization rates may not limit beam losses for 1.06 μm and 1.56 μm high power lasers, they may be significant for three-photon processes when tuned near the D1 and D2 resonances of the

[xvi] The single factor of e has been left in the denominator to make calculations easier with U_i in eV.
[xvii] Note that due to resonance enhancement, the Doppler shift must be accounted for in calculations.

alkali metals.

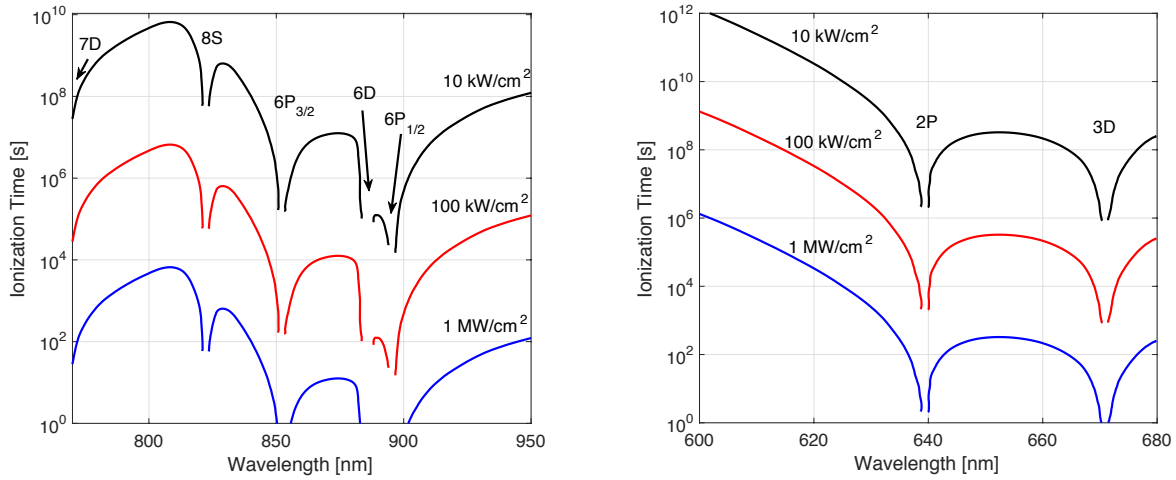

Figure 12: Ionization time t_i as a function of wavelength for cesium (left) and lithium (right) in the vicinity of the D1 and D2 resonances. No calculation results were available near resonances where the curves end discontinuously.

2.3.4 Gravity and Fictitious Forces

Finally, in our discussion of perturbing influences, we must consider reference frame effects and gravity on the combined beam system. The problem is shown in Fig. 13. Subject to a constant acceleration perpendicular to the beam, the photons, particles and spacecraft will all follow different trajectories. For constant velocity motion in z, the trajectory of the particles is parabolic with a radius of curvature,

$$R_c = v_b^2/a_\perp, \tag{46}$$

where $a_\perp$ is the component of acceleration perpendicular to the beam [xviii]. In Sec. 2.3.5 we consider the problem of the spacecraft walk-off of the beam and the feasibility of "beam-riding". In what follows, we focus on the laser and particle beams.

As a thought experiment, consider the two limiting cases of the equations of coupled propagation: 1) when the laser intensity is very low $|U| << k_b T_\perp$, and 2) when the particle density is very low $V << 1$. In the first scenario, the particles are completely unconfined and follow the parabolic trajectory outlined above. Provided $V \sim 2$, the weak laser will follow the particle beam just as in a curved fiber optic cable. In the second scenario, the laser effectively traps particles but the particle density is insufficient for guiding.

We first consider scenario (1). In a frame of reference fixed to the initial beam direction,

[xviii] Note that for light Eq. 46 would be incorrect. Famously, general relativity predicts a the deviation angle of light around a gravitating object is a factor of 2 larger than the Newtonian prediction [71].

the particle kinematics can be modeled by adding to the dipole potential a linear potential associated with the transverse acceleration,

$$U_b(x) = -m_a a_\perp x. \tag{47}$$

This "bending potential" distorts the potential well induced by the laser, as shown in Fig. 14, and produce an asymmetric particle density profile and increased escape losses, which will depend on the relative bending and trap depth. As an example, we consider the gravitational acceleration of the sun at 1 AU: 5.93 mm/s ^{2}. Over a distance of 0.5 meter, this results in a potential energy difference corresponding to 2.5 μK (^{7}Li) or 47 μK (^{133}Cs), which are comparable to the temperatures obtained by laser cooling (Table 1).

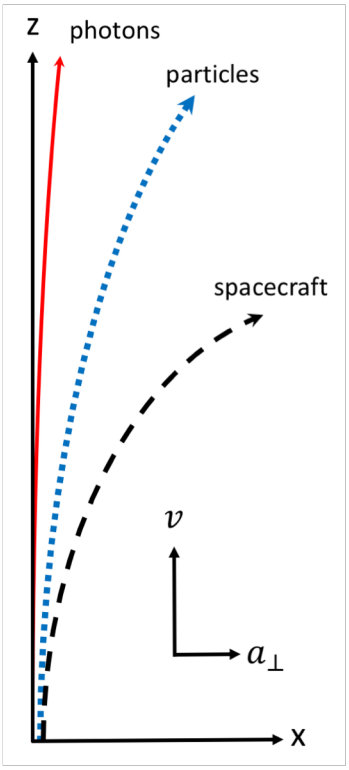

Figure 13: Bending of the laser, particle and spacecraft trajectories due to gravity and centrifugal forces, perpendicular to the nominal beam direction. The relative bending has been greatly exaggerated.

In the above, we considered the effect of bending from the particle perspective in scenario (1). Now, we consider scenario (2) from the perspective laser beam. In this case, the particles are bending on a parabolic trajectory and we ignore the growth of the beam width due to the finite divergence angle Ω. Under this assumption, the problem is analogous to bending losses in a large mode-area fiber optic waveguide. It is clear from the widespread use of fiber optic cable that for certain amounts of bending, fiber is able to guide the laser around the bend with little loss. However, as the size of the waveguide core becomes larger and the refractive index contrast ($\delta\eta$) becomes smaller (at constant V-parameter), the light will eventually be unable to follow the bend and significant bending losses will result [72].

In order to estimate the tolerable bending, we appeal to the well-developed theory of light propagation through curved (i.e. spooled) fiber optic waveguides based on an analytical approach known as the effective index method [73, 74, 75]. The method incorporates the differential path length through the bent fiber as a linear refractive index gradient, analogous to the previously introduced bending potential.

Bending losses in large mode area waveguides, which utilize a large core size and refractive index gradient, have been analyzed using this method by Fini [72]. The threshold for substantial bending loss was shown to be given by a bending sensitivity parameter S [meter],

$$S = \frac{\eta a}{\delta\eta_{eff}} \approx \frac{4a}{\delta\eta} \tag{48}$$

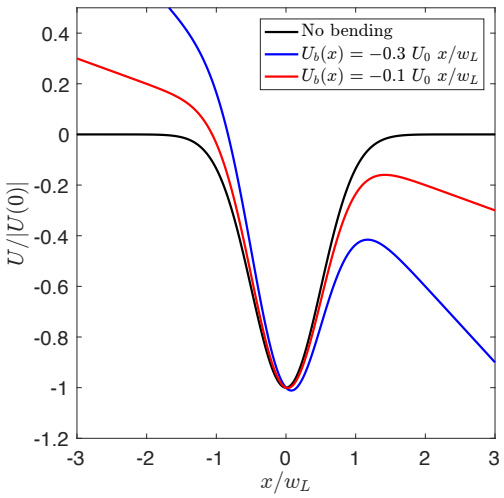

Figure 14: Distortion of the trapping potential due to transverse accelerations.

where $\delta\eta_{eff}$ is the *effective* index contrast, which is related to $\delta\eta$ but modified for each particular waveguide mode and is V-number dependent [52]. The approximation shown in Eq. 48 holds for our weakly guiding beam ($\eta \sim 1$) for the fundamental (LP_{01}) mode when $V = 2$. The allowable bend radius is related to S by $S \geq R_c$ [72], which using Eq. 18 we obtain an expression for the minimum radius of curvature that allows guiding:

$$R_c \geq \frac{4r_n A_p}{K\lambda^2} \approx \frac{2r_n^3}{\lambda^2} \tag{49}$$

where r_n is the particle beam radius we have used $V \approx 2$. Notably, the allowable curvature scales with the third power of the particle beam radius. Again taking the example of the solar gravitational acceleration and a beam traveling at $0.1c$, we find $R_c = 10^6$ AU. While this appears enormous, the short wavelength of light results in an allowable beam radius of $r_n = 42$ meters. For a slower beam, $v_b = 300$ km/s, the maximum radius is 2 meters, close to the optimum beam size based on other considerations.

In the above discussion bending estimates were made based on the solar gravitational acceleration at 1 AU. The actual transverse acceleration will depend on the specific transmitter orbit and reference frame. If the transmitter not only orbits a celestial body but also rotates, light and particles will experience an acceleration $\mathbf{a}_f$, in addition to gravity, associated with Coriolis and centrifugal forces,

$$\mathbf{a}_f = -2\ \boldsymbol{\Omega}\times\mathbf{v} - \boldsymbol{\Omega}\times\boldsymbol{\Omega}\times\mathbf{r}_t \tag{50}$$

where $\mathbf{r}_t$ is the vector from the center of rotation to the transmitter and $\boldsymbol{\Omega}$ is the orbital and rotational angular frequency. For high energy particle beams, Coriolis forces can produce accelerations so large that the self-guided beam is nearly unfeasible. Instead, a transmitter in orbit but with fixed attitude relative to the celestial sphere results in more tractable accelerations. *In this case, only the centrifugal force (second term in Eq. 50) is present.* In what follows, we consider a reference frame fixed relative to the transmitter spacecraft attitude.

For a transmitter at the earth-sun Lagrange points (e.g. L1 or L2), with fixed attitude with respect to the celestial sphere, the particle beam experiences a centrifugal acceleration given by $\left(\frac{2\pi}{1\ \mathrm{year}}\right)^2 \times 1\ \mathrm{AU}\ \hat{\mathbf{r}} = 5.93\ \mathrm{mm/s}^2\ \hat{\mathbf{r}}$. Note that the centrifugal term does not depend on location or velocity and that it is precisely balanced by gravity at the transmitter location. As the particle beam moves away from the transmitter, this balance is upset by the changing distance to the sun

and orientation relative to the sun and transmitter.

Fig. 15 illustrates several potential locations for the transmitter in nearby cislunar space. In addition, we also consider geosynchronous orbit. These locations are attractive for practical reasons of deployment, servicing and short communications delay. Their quiet thermal and gravitational environment also enables ultra-stable pointing. For example, preliminary analysis of the Luvoir telescope line-of-sight stability shows a rms pointing error of order 1 micro-arcsec may be achievable, limited by the reaction wheel disturbances and depending on their speed [76]. For reference, this pointing error corresponds to hitting a 0.73 m target at 1 AU. Although well beyond the Luvoir specification (0.3 masec rms), this estimated stability demonstrates the potential for achieving the high pointing accuracy required for beamed propulsion generally and self-guided beams in particular.

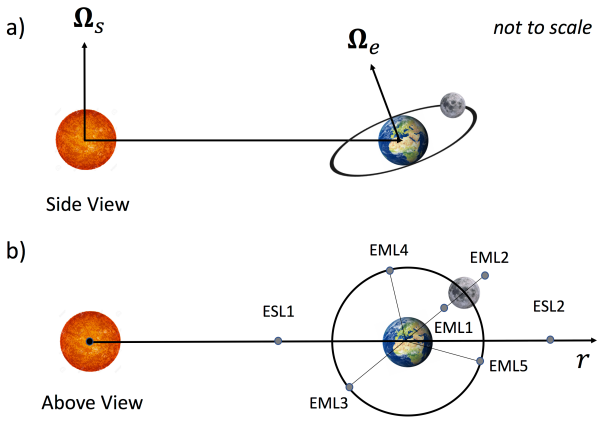

Figure 15: Beam system locations in extended cis-lunar space.

Finally, we consider the limitation of the beam diameter, based on the allowable bend radius, for different transmitter locations. Since the centrifugal acceleration due to the solar orbit is greater than that from a lunar orbit, we also estimate the bend radius from the earth-moon Lagrange points using the sun-earth centrifugal acceleration. For geosynchronous orbit, the centrifugal acceleration is 0.189 m/s ^{2}. Allowable beam diameters, calculated from Eq. 48, are shown in Fig. 16 as a function of v_b from 10 km/s to $0.3c$. The results show that light may be guided around even low velocity beams, provided they are narrower than several tens of centimeters. For high velocity beams, such as for the interstellar mission, even transmission from GEO may be feasible. It should be noted that the above represent a worst-case estimate, as gravitational forces will largely cancel the centrifugal force while the particle beam is within ~ 1 orbital radius of the transmitter.

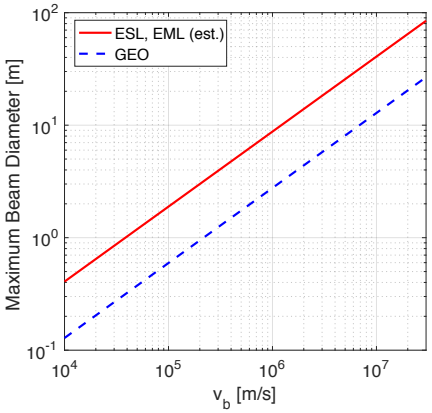

Figure 16: Allowable beam diameter as a function of beam velocity, from Eq. 49 and Eq. 46.

2.3.5 Transmitter Location and Beam Riding

In the previous section, we considered Fig. 15 and limiting cases where particles would follow the laser beam path and the laser would be guided along the particle beam path. In this section we return to the problem of the spacecraft trajectory and maintaining alignment with the beams. While laser propulsion concepts have proposed actively targeting the spacecraft using a phased laser array, such an approach is not feasible here, since the particles and photons travel at different speeds. Instead, we consider fixing the beam pointing and requiring that the spacecraft

follow the beam trajectory, also known as "beam riding" [28, 77].

Beam riding requires the generation of thrust, perpendicular to the z-axis, to maintain spacecraft motion along the beam trajectory. Mathematically, this amounts to equating the local radius of curvature of the beam trajectory with that of the spacecraft. From Eq. 49,

$$\frac{v_b^2}{a_\perp} = \frac{v_{sc}^2}{a_\perp + a_{br}} \tag{51}$$

where a_{br} is the acceleration required for beam-riding, which by re-arranging Eq. 51 can be expressed as,

$$a_{br} = a_\perp \left[\left(\frac{v_{sc}}{v_b} \right)^2 - 1 \right]. \tag{52}$$

The necessary acceleration is maximum at zero spacecraft velocity, with a maximum value of $a_\perp$ (which includes partially offsetting gravitational and centrifugal terms) and goes to zero as $v_{sc} \rightarrow v_b$. Considering that initially, at the transmitter location, gravity and centrifugal terms balance, one might expect that a_{br} upon detailed calculation a local maximum, substantially less than $a_\perp$, may result as the spacecraft accelerates to v_b. again consider the ESL transmitter location, where we approximate $a_\perp \sim 5.93$ mm/s^2 as a worst-case scenario.

The Δv required to follow the beam depends on the time the spacecraft spends accelerating, while the thrust requirement is determined from $a_\perp$ and payload mass. In Sec. 3, we find typical acceleration times range from $10^3 - 2{\times}10^4$ seconds, for which the required $\Delta v = a_\perp t = 5.9 - 108$ m/s. For a 1 kg spacecraft, the thrust requirement is 5.93 mN, which could be achieved with a micro-propulsion system, such as field-emission electric propulsion or colloid thrusters [78], or even cold gas thrusters. Alternatively, even a small degree of control authority over the light or particle beam thrust vector would prove sufficient for beam riding. In conclusion, while systems for beam-riding must be incorporated into the spacecraft design, they do not appear to be prohibitive.

3 Mission Design

In previous sections the conditions for self-guiding and an array of relevant physical processes were investigated. Here, we apply those principles to space propulsion and develop a framework for optimizing of the beam parameters, such as beam velocity, area, density, etc. (see Fig. 5), subject to applicable constraints. The optimization framework is first applied towards optimizing a self-guided beam system for a Proxima b flyby mission at $0.1c$, with a total beam power $P_t = P_L + P_p$ of 50 GW. Later, we examine how variation in these constraints affect probe mass and furthermore consider a mission to the solar gravitational lens point at 550 AU. In all cases, we use a non-relativistic model the particle and spacecraft dynamics, though Doppler shifts are taken to account when calculating the atomic polarizability, scattering rates and laser thrust.

3.1 Brightness: A Key Parameter

The self-guided beam system contains a wide array of parameters which all affect the overall propulsion performance. In this section, we reduce the parameter space to a single key property of the particle beam known as the brightness. To motivate this conclusion, we begin by considering the trapping constraint: that the dipole potential must be deep enough to contain the particles. In Sec. 1.3, we found that a good approximation is $|U(0)| = 4k_bT_\perp$ corresponding to beam areas $A_L = 4A_p$. Using these relationships and Eq. 22, the total laser beam power ($P_L = 1/2 I_L A_L$) can be rewritten in terms of the particle beam area and transverse temperature. Taking the ratio with the particle beam power (Eq. 7), we arrive at,

$$\frac{P_p}{P_L} = \frac{B}{B^*} \quad E_k[\mathrm{MeV}] \quad \alpha_v[\mathrm{nm}^3], \tag{53}$$

where B is the reduced brightness [32, 79, 80, 81] (hereafter referred to simply as "brightness"),

$$B = \frac{e\dot{m} \;/\; m_a}{\Pi \; E_k} \tag{54}$$

and,

$$B^* = \frac{4ec}{\pi^2 \times 1\mathrm{nm}^3 \times 1\mathrm{MeV}} = 9.73\times10^9 \ \mathrm{A/m^2/sr/eV} \tag{55}$$

is a characteristic value of brightness [xix]. The importance of Eq. 53 is difficult to understate, as it shows that only a small number of parameters influence the division of power between the laser and particle beams, subject to the self-guiding conditions. In what follows, we discuss the role of brightness.

Briefly, brightness is the beam current [xx] normalized by the area, divergence solid angle and particle energy. Rather than the phase space volume (Π), brightness is a measure of the phase space density. With a brighter beam, more mass flow can be directed onto a spot size at a distance. The brightness is a more useful metric of beam performance than the area-divergence product,

[xix] 1 MeV and 1 nm^3 were chosen as typical values of the particle energy and volume polarizability.

[xx] The equivalent current, as Eq. 54 shows, can be computed for a neutral beam by multiplying the mass flow rate by e/m_a.

since a small value of Π is not practically useful if the mass flow rate is miniscule. As we will demonstrate, the particle beam brightness has a significant impact on the overall performance of self-guiding.

As discussed in Sec. 1.3, a higher thrust-to-power ratio is derived from the particle beam, and thus maximizing the ratio P_p/P_L maximizes the thrust of the combined, self-guided beam. Eq. 53 then demonstrates that two modes of operation are possible, depending on B:

- $P_p << P_L$: Thrust principally derives from the photons and the self-guided mode acts to overcome diffraction. This allows the beam to propagate further with a small transmitter aperture.

- $P_p \geq P_L$: Thrust principally derives from the particles, *in addition to self-guided laser and particle propagation.*

While both modes of propulsion exhibit self-guiding, the greatest performance is obtained in the latter mode, which relies on a sufficiently bright atomic beam.

3.2 Optimization Framework for Self-Guided Beamed Propulsion

We now present a beam optimization and mission design framework. Taking into consideration the guiding and trapping conditions and relevant loss processes, we proceed to develop an optimization methodology.

The primary external inputs are the beam brightness B, total power $P_t = P_L + P_p$, and final velocity, v_f. The beam area, which is notably unconstrained by the light guiding and particle trapping conditions, is arbitrarily set to $A_p = 1$ m^2, consistent with the bending constraint in Sec. 2.3.4. Although the area directly affects the collision rate, we find that in nearly all cases distance is limited by stochastic heating.

The following analysis studies the sensitivity of payload mass to particle beam velocity and alkali metal species. Light guiding and particle trapping constraints are enforced through two equations: Eq. 53, which was derived from the trapping condition $|U(0)| = 4k_bT_\perp$, and Eq. 18, which using Eq. 19 and Eq. 56 can be recast as,

$$P_p = \frac{E_k v_b V^2 \lambda^2}{8\pi^2 \alpha_v(\lambda)}. \tag{56}$$

These two equations, along with $P_t = P_L + P_p$, constitute three equations for four unknowns, P_L, P_p, λ and v_b. We choose to cycle through a range of v_b, with $v_b > v_f$ in all cases, and compute the maximum payload mass for each choice of v_b.

The procedure, shown in Fig. 17, is briefly described. First, λ is obtained from these euqations by analytic elimination of P_p and P_L and root-finding of the resulting transcendental equation. From λ, other parameters (such as the polarizability) are calculated and the beam

propagation distance is determined from the propagation limiting phenomena, which may include Rayleigh scattering (Sec. 2.3.1), multi-photon ionization (Sec. 2.3.3), collisions (Sec. 2.3.2), or heating (Sec. 2.2.3). In practice, we find that heating (Eq. 25) imposes the dominant limitation while collisions between beam particles may also be important. The flexibility in choosing the beam area, subject to the maximum limits of light guiding (Sec. 2.3.4), usually allow the collision rate to be reduced below the heating constraint.

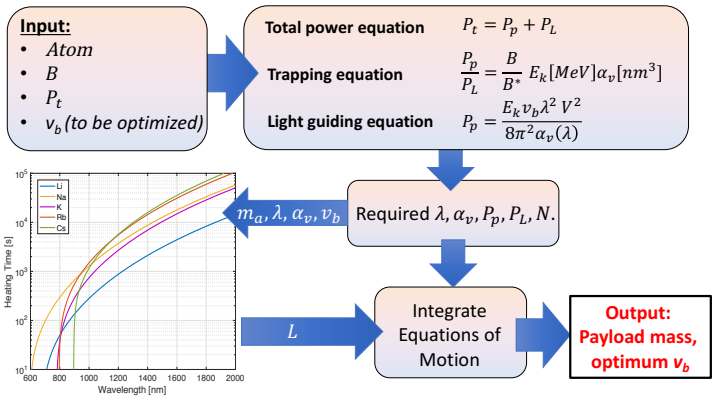

Figure 17: Block diagram of the beam parameter optimization procedure.

Finally, the propagation distance is determined by $L = v_b t_h$. The maximum payload is calculated by integrating the spacecraft equation of motion, given by Eq. 9, Eq. 6 and Eq. 28, for different values of the spacecraft mass until one is found such that $v_{sc} = v_f$ at $z = L$. The process is then repeated for various particle beam velocities.

3.3 Proxima b Flyby Mission

Calculated parameters for the Proxima b flyby mission are plotted in Fig. 18 as a function of the beam velocity normalized to $v_f = 0.1c$. These include the duration the spacecraft accelerates in the beam (2,2), energy efficiency (2,3 - spacecraft kinetic energy divided by total expended beam energy), and fuel consumption (3,2 - mass flow rate integrated over the acceleration time). For inputs, we have taken $B = 5{\times}10^7$ A/m^2/sr/eV, which is only slightly above systems that have been reported [29].

We begin by commenting on several trends observed as the beam velocity is increased. In frame (1,1), we see the optimum wavelength shifts to the visible in order to meet the light-guiding condition, as higher velocity requires a reduced mass flow rate (panel 3,1) and density (panel 1,2) at constant power. As a consequence of increasing the polarizability, the heating time decreases (1,3) and the propagation distance decreases (2,1). The optimum condition for payload mass is obtained at a value of v_b somewhat higher than v_f, since the particle beam thrust (Eq. 9) considerably reduces as v_{sc} approaches v_b.

The various alkali elements exhibit a notable trend, with the largest payload obtained with the heaviest elements. Cesium shows the best performance, though rubidium and potassium are only a factor of approximately 2 and 3 lower, respectively. The mass trend can be understood to result from the scaling of E_k with m_a at constant velocity, and therefore lighter elements have a lower ratio P_p/P_L (through Eq. 53) and therefore thrust.

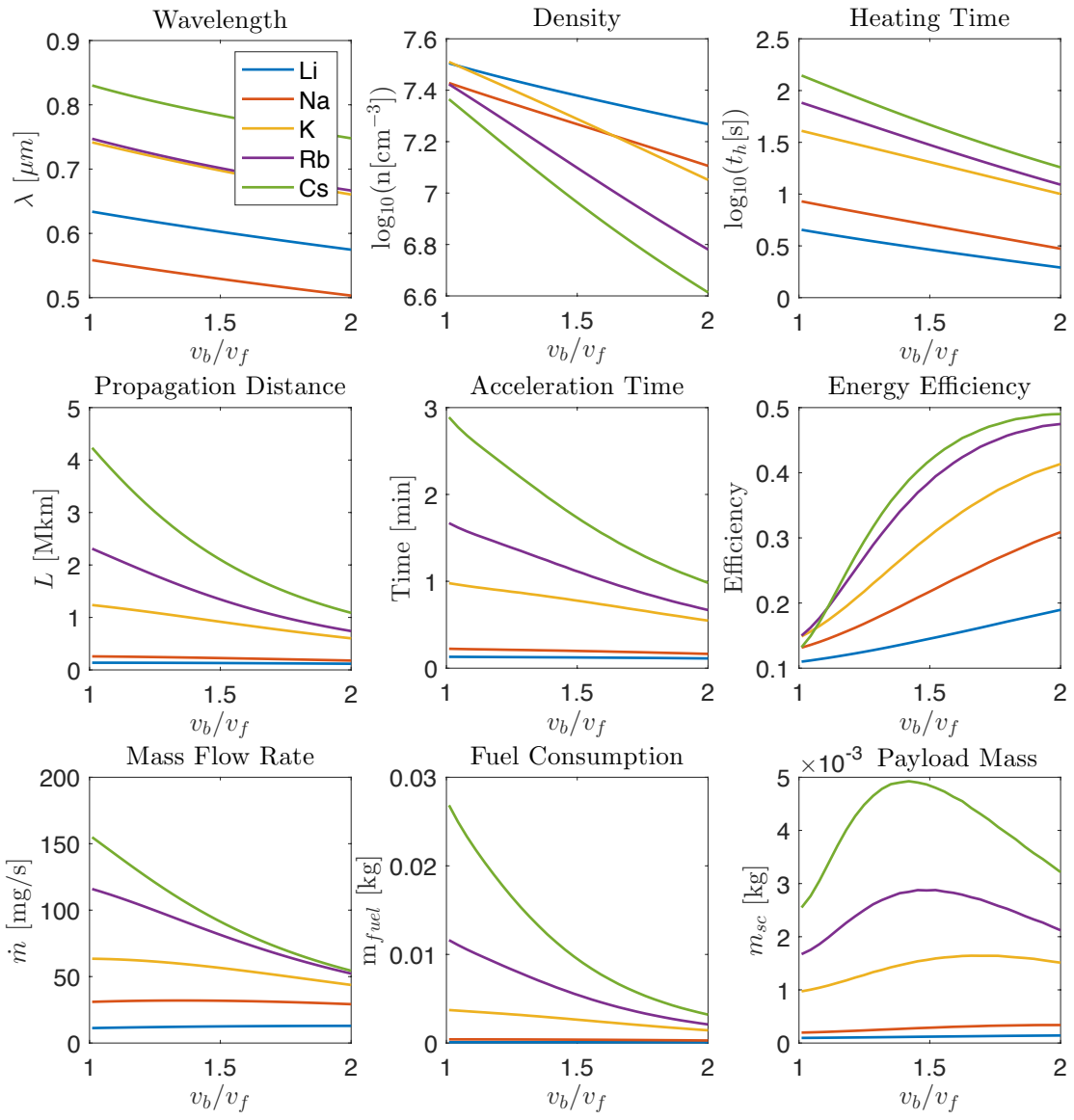

Figure 18: Proxima b mission design: $P_t = 50$ GW, $B = 5{\times}10^7$ A/m^2/sr/eV.

The optimized payload of 5 grams is similar or slightly higher than that achieved by laser propulsion concepts (~ 2 grams [14]). Likely, this mass is insufficient considering that additional subsystems are required to accommodate the particle flux and thrust transfer to the spacecraft, which are yet to be considered. However, we note that achieiving such a payload with a 1 m^2 transmitter rather than a large-scale phased array of order 10 km^2 conveys system-level benefits which are hard to quantify. Moreover, many authors have noted that particle beam energy efficiency is potentially much higher ($\sim$ 90% [82, 83, 84]) in comparison with lasers ($\sim$ 45%), which also results in less heat rejection to space. Quantifying these trade-offs is deferred to a future economic analysis.

In order to better explore the scaling laws of the self-guided beam system, calculations

were performed for a 100 GW power budget over a range of brightness and final velocity: specifically, a 0.075c flyby (60.5-year mission duration) and a 0.044c flyby (100-year mission duration) with a range of brightness from $B = 5\times10^{7} - 5\times10^{12}$ A/m^2/sr/eV. The resulting parametric analysis is summarized in Fig. 19, where the optimum alkali atom is indicated next to each data point.

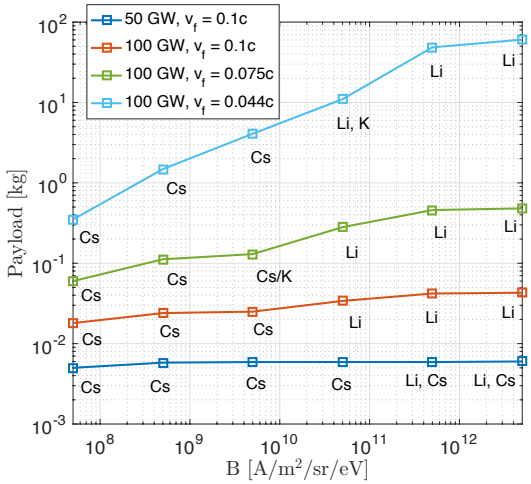

Figure 19: Payload scaling with beam brightness, final velocity, and power. Optimal atomic species are labeled.

Looking at the 0.1c missions for 50 GW and 100 GW power, we observe that the power doubling results in a 4 - 5 times increase in payload, from 5 mg to over 40 mg at high brightness. The velocity scaling at a fixed 100 GW beam power is dramatic. For a brightness of 5×10^{12} A/m^2/sr/eV, the payload increases from 5 mg to approximately 60 kg as the velocity is reduced from 0.1c to 0.044c, consistent with a velocity scaling of approximately $\sim v_f^{8.8}$. The strong scaling arises from Eq. (56) and the need for a large polarizability (and commensurate short t_h) when the beam power is low. At the lower range of brightness, the velocity scaling is markedly weaker, approximately $v_f^{3.5}$. From this study, we conclude that bright atomic beams are critical for maximizing payload capability. The higher scaling above $B \sim 5\times10^{10}$ A/m^2/sr/eV demonstrates the relevance of the characteristic brightness introduced in Eq. 55.

Finally, we note that above $B \sim 5\times10^{10}$ A/m^2/sr/eV an improvement in payload is observed using Li rather than Cs as the "propellant". This occurs because at sufficiently high brightness $P_p >> P_L$ and, as a result of its larger polarizability to mass ratio, the beam satisfies the light guiding condition at a reduced mass flow rate. In summary, analysis of the interstellar mission shows that bright atomic beams are needed for reasonable payload and that slight reductions in mission duration can result in payloads in the range of 1 - 10 kg.

3.4 Solar Gravity Lens Mission

The interstellar mission discussed in the previous section pushes the limits of the self-guided beam system under the imposed power and velocity constraints. In order to examine nearer-term capabilities, we also analyze a solar gravitational lens mission. Such a mission aims to utilize the bending of light from the sun to image distant objects, such as extra-solar planets, requiring the spacecraft be positioned 550 AU or farther from the sun opposite the target [85].

We consider a 15-year mission profile with acceleration by the self-guided beam followed by a 13-year cruise to 550 AU at 200 km/s and 2 years of science as the spacecraft drifts from 550 AU to 634 AU. First, we consider fixed system inputs: 200 MW of total power and a brightness of $B = 5\times10^{9}$ A/m^2/sr/eV. Under these constraints, the self-guided beam parameters are shown in Fig. 20.

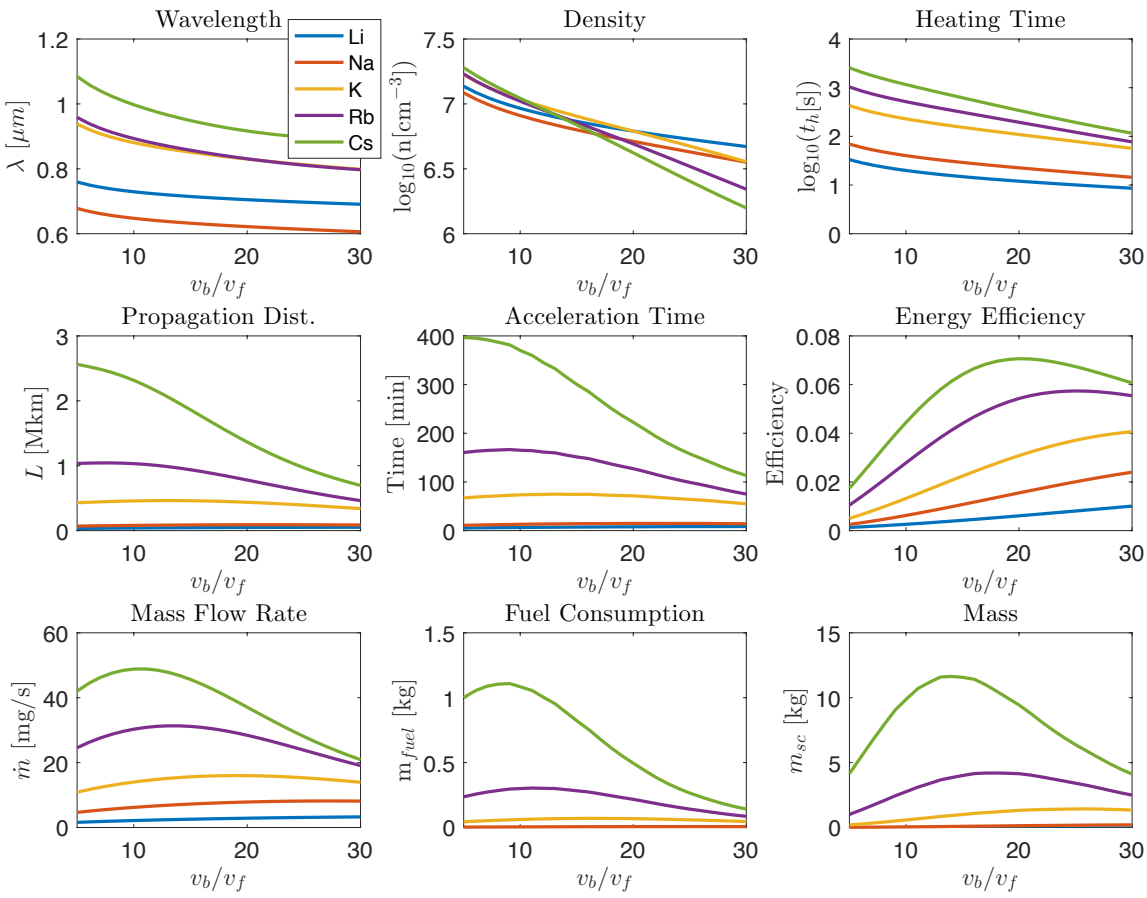

Figure 20: Optimization of beam parameters for the solar gravitational lens mission, $v_f = 200$ km/s, $B = 5{\times}10^9$ A/m^2/sr/eV, $P_t = 200$ MW.

The optimization results in a maximum payload of 11.5 kg using a cesium atomic beam. As with the interstellar mission, increasing beam velocity requires tuning closer to atomic resonances and consequently reduced heating time and propagation distance. The optimum beam velocity is $0.0085c$ and results in a propagation distance of about 2 million km (0.013 AU). For comparison, striking the same 1m^2 target with a laser requires a 2.2 km diameter aperture or, by particle beam, a transverse temperature of 25 nK. Compared with the free propagation of the laser or particle beams which make up the system, the distance gain from self-guiding is approximately a factor of $10^2 - 10^3$.

In order to explore the power and brightness dependence on the payload mass, a parametric study was performed over a range of brightness from $5{\times}10^7 - 5{\times}10^{10}$ A/m^2/sr/eV and power levels of 20 MW, 50 MW and 200 MW. The results are depicted in Fig. 21. Note that over the lower range of brightness the payload mass exhibits exhibits a power law scaling slightly stronger than $\sqrt{B}$. Once the beam brightness becomes larger than B^* the slope displays a noticeable increase. From Eq. 53, we interpret this as resulting from a shift from primarily laser-derived thrust

to particle-derived thrust. Overall, we find that masses on the order of the New Horizons spacecraft (payload mass $\sim$ 30 kg) require power levels of order 100 kW combined with particle beam brightness greater than 10^{10} A/m ^{2}/sr/eV.

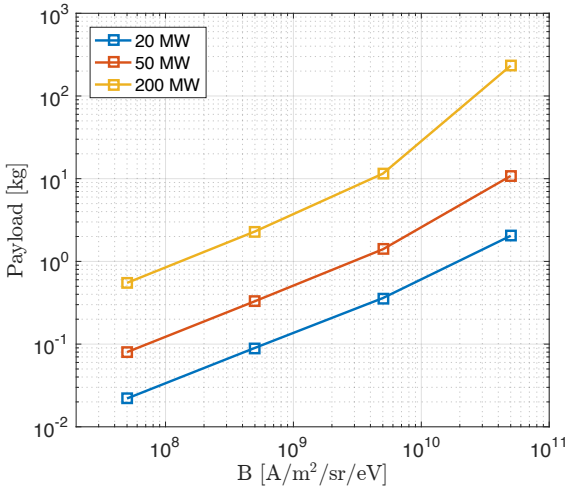

Figure 21: Parametric study of payload mass for the gravitational lens mission, $v_f = 200$ km/s.

In summary, this section presented an analysis of self-guided propulsion and estimates of the payload capability using a beam optimization framework. The results suggest that while the initial 50 GW, $0.1c$ mission would reflect only a small benefit from self-guided propulsion, there are still system-level benefits, such as reduced transmitter size, which remain to be quantified. The strong velocity and power scaling (even stronger than laser propulsion) also enables substantial payload capacity for a slightly longer mission. Scaling to lower velocity missions appears quite favorable, enabling high speed missions to the solar gravitational lens, and generally throughout the solar system, with power levels on the order of 100 MW. Critically, these performance figures are all based on achieving a beam brightness of order of $10^{10} - 10^{11}$ A/m ^{2}/sr/eV or higher, the feasibility of which is discussed in Sec. 5.

4 Numerical Simulation

In this section, we return to the governing equations discussed in Sec. 2 and begin developing numerical techniques for their solution. For non-relativistic motion, the particles obey Newton's equations of motion (Eq. 28 or Eq. 29), subject to the dipole potential (Eq. 22), stochastic scattering impulses of $\hbar k$ occurring at a rate R_{sc} (Sec. 1.3), and collisions (Sec. 2.3.2). For the laser beam, propagation of a weakly guided, linearly polarized and monochromatic beam is described by the paraxial Helmholtz equation, Eq. 16. A block diagram illustrating the equations and coupling is shown in Fig. 22.

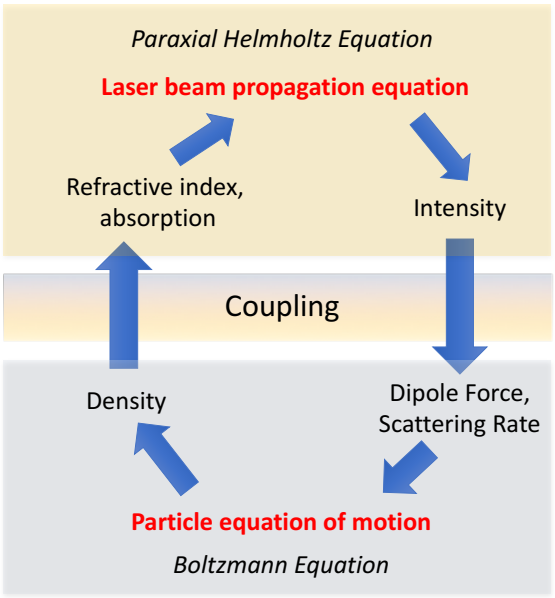

Figure 22: Equations for the field (above) and particles (below) and sources of coupling.

The particles and fields are nonlinearly coupled through the density-dependent refractive index and the intensity-dependent dipole force. For the former, attenuation is included in the usual way through the imaginary part of the refractive index,

$$\eta^2 - 1 = n\left[2\pi\alpha_v + i\frac{\sigma_R}{2k_0}\right]. \tag{57}$$

The dipole force is calculated from the optical field amplitude $\bar{E}$ by,

$$\mathbf{F}_{dip} = \frac{2\pi}{c}\alpha_v \nabla \bar{E}^2 \tag{58}$$

while the scattering rate is determined from energy conservation,

$$R_{sc} = \frac{I\sigma_R}{\hbar\omega_L}. \tag{59}$$

These equations, along with a collision model, completely describe the evolution of the coupled system. Simulation of the fully coupled equations is outside the scope of Phase I and here we examine the uncoupled system.

The challenges to solving these equations are multifaceted: the stability characteristics of the coupled equations are unknown and the domain aspect ratio is very high (e.g. 10 m ^{2} × 0.1 AU). Careful consideration of the numerical methods and boundary conditions is required for accurate, high fidelity simulation. Below, we present initial steps made toward high fidelity simulations in an axi-symmetric geometry. In Phase I, we have developed and partially verified simulation tools for uncoupled propagation of the optical field and particles.

4.1 Beam Propagation

Propagation of the optical field is an initial value problem, where an electric field profile, initially defined at the transmitter plane, is propagated through space. Unlike free-space propagation, the solution technique must allow for an inhomogenous medium, with spatially varying refractive index. A commonly applied method for nonlinear beam propagation is the split-step method, which is based on an operator splitting scheme. In this approach, the linear or nonlinear phase shift imparted by the medium is alternated with a fourier propagation technique. The problem with this technique, or any based on spectral methods, is proper treatment of the boundary condition. Laser energy must be allowed to flow out of the boundary, without reflection, due to the extremely high aspect ratio of the domain. While perfectly matched layers provide one option, we have adopted an analytical approach based on the adaptive transparent boundary condition method of Hadley [86].

In brief, we describe the solution method. For the overall solution, Crank-Nicholson method is applied with spatial derivatives replaced by second order, centered finite differences, with trapezoidal integration in z. Fast inversion of the resulting tri-diagonal matrix is performed using the Thomas algorithm. Like the heat equation, the paraxial wave equation is parabolic and numerical stability is ensured while $\lambda\Delta z/8\pi(\Delta r)^2 < 1$, Δr is the grid size in the radial direction and Δz is the step size in z. In other words, the maximum step size is limited to $\Delta z \leq 8\pi(\Delta r)^2/\lambda$. For large beams, where Δr may be of order 1 cm, large step sizes of order several km are permitted, enabling ultra-long distance propagation using only a standard personal computer. The transparent boundary condition is formulated by determining the local propagation constant and updating the boundary cells based on a local plane wave solution. This ensures energy locally propagates out of the domain. In the following, we describe verification and exploratory studies with this code.

4.2 Verification

Verification of the beam propagation code is performed by comparison with the Gaussian beam solution, an exact solution of the paraxial wave equation in vacuum [36]. For simulations, the beam waist is located at the transmitter, resulting in no complex phase shift across the beam profile. The Gaussian solution is then given by,

$$\bar{E}_g = \frac{w_L}{w(z)} \exp\left[-\frac{r^2}{w(z)^2}\right] \exp\left[-i\left(kz + k\frac{r^2}{2R(z)} - \psi(z)\right)\right] \tag{60}$$

where the beam width and radius of curvature functions are given by $w(z) = w_L\sqrt{1 + (z/z_r)^2}$ and $R(z) = z(z + (z_r/z)^2)$, where $z_r = \pi w_L^2/\lambda$ is the confocal beam parameter. A beam, with an initial width of $w_L = 4$ m, was numerically propagated over 320,000 km (0.0021 AU) using 800 grid points in r and 10,000 grid points in z. A comparison of the calculated intensity profile and the analytic solution is displayed in Fig. 23 (right) and exhibits excellent agreement at 0.32 million km. A grid study was also performed, demonstrating a convergence of numerical errors towards zero as Δr was reduced by factors of 2 and 4.

Exploratory studies were performed on the application to light guiding in a non-uniform

medium. For the density profile, we considered a gaussian distribution with a) fixed width equal to the laser intensity profile, and b) increasing width, corresponding to a divergence angle 10× less than the laser beam. In both cases, the peak initial density was set to the critical density obtained by application of Eq. 19 for a lithium atomic beam at a wavelength of 1 micron. The results of beam propagation are shown in Fig. 24. They demonstrate that even as the beam expands light guiding can be maintained over large distances, as expected based on previous discussion of the V-parameter in Sec. 2.2.1.

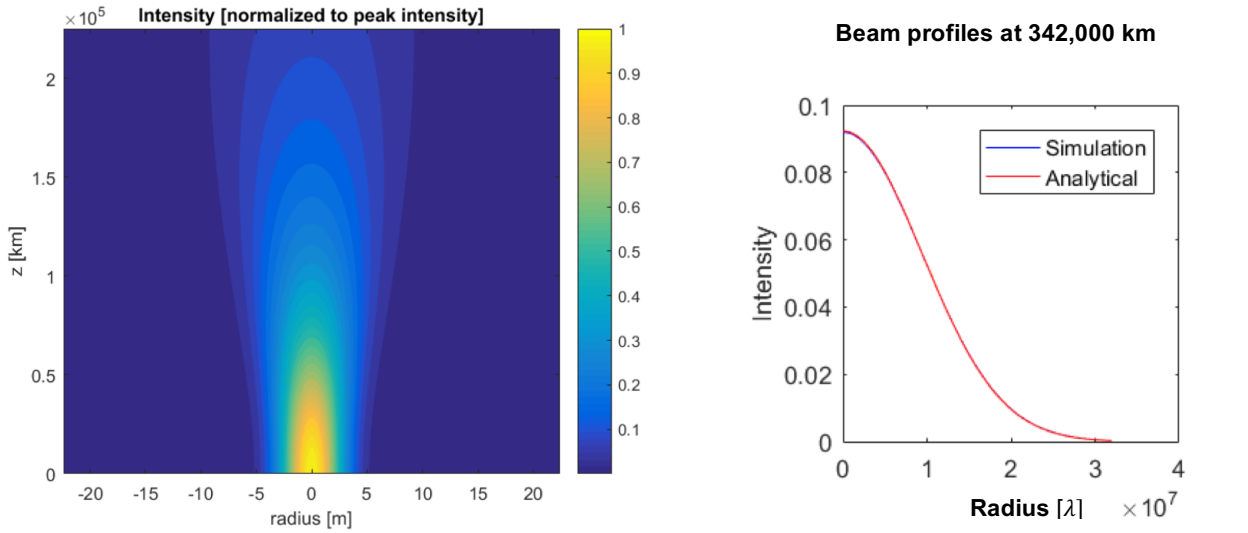

Figure 23: Code verification with Gaussian beam in free space, showing 2D intensity profile (left) and comparison with analytical solution (right).

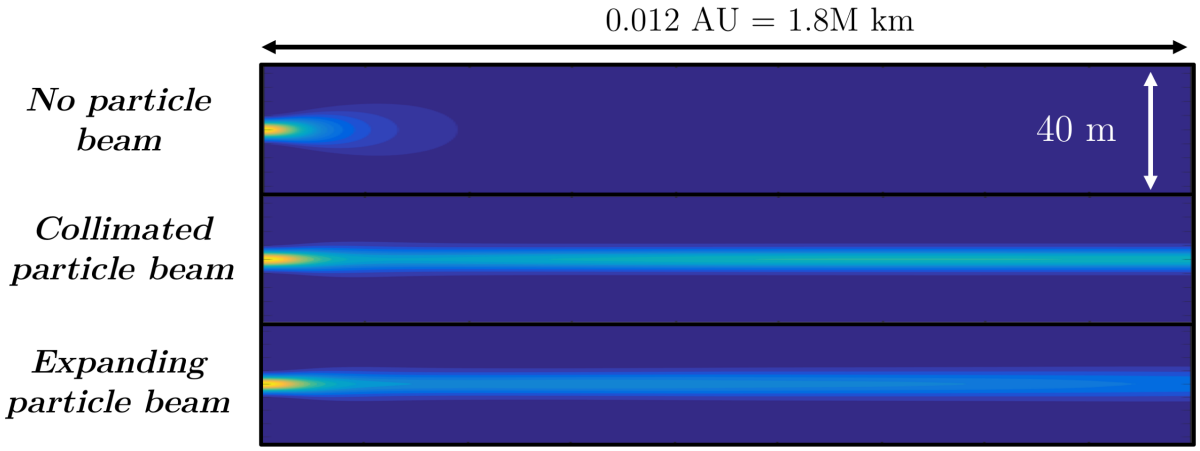

Figure 24: Comparison of three scenarios: a) beam propagation in vacuum, b) beam propagation through a collimated (zero temperature) particle beam, c) propagation through an expanding particle beam.

In summary, the simulation tool has been verified and exhibits excellent performance for propagation in free space and inhomogenous media. Future integration with high performance computing resources will easily permit simulations over distances of order 1 AU. We have also

implemented the exact analytical density profile for a collisionless particle beam expanding in vacuum, as described in [87]. In the future, we plan to examine beam propagation through these particle beam profiles for applications to propulsion, energy transfer and communications.

4.3 Particle and Coupled Simulation

Particle simulation development during Phase I has adopted the following strategy: (i) develop and verify the particle mover under planar geometry, (ii) develop a particle mover for cylindrical geometry, and (iii) couple the particle simulation with the light field solver.

First, the test case that was chosen for verification of the particle module is a collisionless effusion problem proposed by Cai and Boyd [88], where an analytic solution is derived. The particle update is performed using a leap-frog method, which is a dissipationless scheme, and linear interpolation is used to calculate the number density on the computational nodes. Depending on the particle injection, e.g. slit in the center and two slits off center, the particle density and bulk velocity profiles vary and both cases are reproduced well with our particle simulation. Second, a cylindrical simulation geometry is developed. Here, the force field due to light intensity and centrifugal force are accounted for. Third, the field solver, originally written in MATLAB, has been transferred to C and is currently coupled with the particle simulation. The complete simulation, in which the light field and particle solvers are fully coupled, is being further developed and tested, with future studies of uncoupled and fully coupled propagation planned.

5 Particle Beam Technology

The mission analysis in Sec. 3 demonstrated that certain particle beam parameters were needed to maximize the potential of self-guided beamed propulsion. In this section, we describe the current status of particle beam technology relative to these requirements. Because laser technology has been extensively discussed in works on laser propulsion (e.g. [89, 4]), we only consider the particle source.

In Sec. 3, we found that one key figure of merit for the self-guided particle beam is its brightness B, with higher brightness enabling increased payload capability. In addition, the beam source must provide a sufficient flow rate (i.e. enough power) to meet the light guiding condition at a given wavelength λ [xxi]. These parameters are on the order of 10^{10} A/m^2/sr/eV and 100 mg/s, respectively. In this section, we address the current technology and future prospect of generating neutral beams with these properties.

5.1 Bright Atomic Beams

Bright atomic beams are produced by maximizing the flux of particles $\dot{m}/A$ or minimizing the area-divergence product Π (see Eq. 54). In contrast with photons, the value of Π for a particle beam can be reduced by the action of dissipative forces and the extraction of entropy from the beam. This was first demonstrated by Chu and co-workers [90] by applying Doppler laser cooling to atomic sodium. A wide array of laser approaches have since been developed for cooling atoms below μK and even nK temperatures.

While the majority of laser cooling is performed on atoms at rest in the laboratory frame, several authors have examined cooling, and also compression (i.e. increasing the flux) of atomic beams. One such scheme, proposed by Sheehy and co-workers (1990), is shown in Fig. 25. An initially high entropy thermal beam of atoms is first collimated by a 2D optical mollasses, and subsequently focused and re-collimated to produce both a high flux and low divergence beam. The authors note that the first cooling stage alone can yield a phase-space compression of 10^4 (i.e. $\Pi' = \Pi \times 10^{-4}$). Cooling in 3D can be achieved by the "moving molasses" technique, which has been demonstrated for cooling of atomic Cs to 45 μK [91] and cooling of a supersonic helium beam [92], among other examples [79, 93].

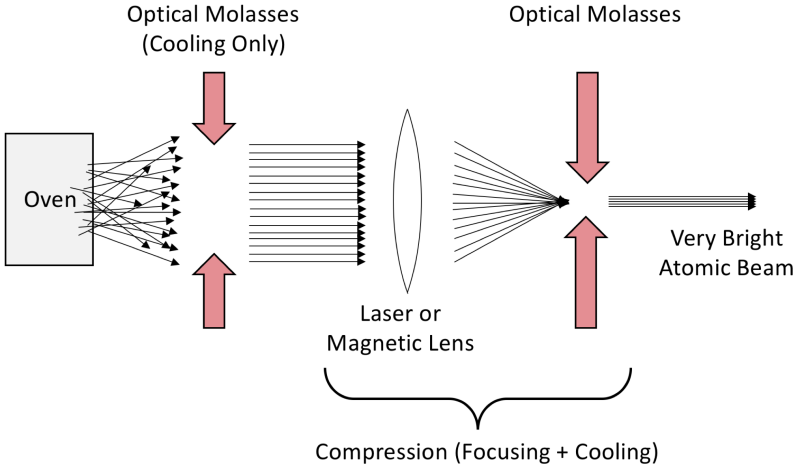

Figure 25: Brightening of an atomic beam by laser cooling, after [94].

[xxi] Note that insufficient flow rate will not preclude self-guiding, but necessitate increasing α_v, reducing t_h and therefore reducing performance.

The brightest atomic beams are currently produced for use in focused-ion-beam (FIB) systems, as described in the book chapter by J.J. McClelland [29] [xxii]. In this application, a cold stream of atoms are photo-ionized and accelerated in an ion optical system. Focusing the beam onto a surface produces local milling and micro-texturing, which can be raster-scanned to create nanostructures. A conceptual cold-atom FIB system layout is shown in Fig. 26. Typically, the ion beam energy is around 30 keV [80]. As in propulsion, minimizing Π allows focusing of the ion beam onto a smaller spot thereby producing smaller micro-features. Moreover, sufficient ion flux is needed produce features in a reasonable time.

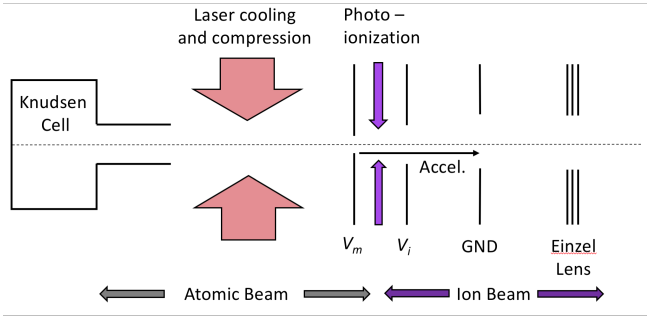

Figure 26: General concept for focused ion beam sources using laser cooling. V_m and V_i denote the maximum and intermediate voltages for ion extraction.

Currently, cold atom FIB sources exhibit brightnesses on the order of 10^7 A/m ^{2} /sr/eV, measured after the ion acceleration stage [95, 96, 80]. Source brightness is currently limited by the mass flow rate into the system and disorder-induced heating, or Boersch effect, that occurs during the ion extraction process [97]. Recent developments using field-ionization rather than photo-ionization have demonstrated the Boersch effect can be suppressed for current densities as high as 0.13 A/m ^{2} [80].

While the current produced in FIB sources is typically small, of order 100 nA [80], the current density corresponds to a cesium mass flux of 0.18 μg/s/m ^{2}. The mass flow rate over a 1 m ^{2} aperture is thus five orders of magnitude below that required for an optimal self-guided beam system, assuming that arraying small sources could be arrayed at a high fill factor.

In summary, FIBs using laser cooled atoms can achieve a brightness of order 10^7 A/m ^{2}/sr/eV. In order to obtain the mass flow rate needed for light guiding, increases in the mass flux (current density) rather than the divergence are required.

5.2 High Current, High Energy Beams

High current ion and neutral beam sources are used in magnetically confined fusion applications for plasma heating [98, 84] and plasma edge diagnostics [99, 100]. The ITER neutral beam source is designed to deliver 16.7 MW of deuterium or hydrogen neutral beam power at an ever of ~ 1 MeV, with a corresponding current density of ~ 200 A/m ^{2}. This current density corresponds to a mass flow rate from 276 mg/m2 (^{133}Cs) to 14.5 mg/m ^{2} (^{7}Li), which is in the required range.

Attaining high current in the ITER neutral beam requires a multi-aperture acceleration grid, due in part to the space-charge effects in the un-neutralized beam characterized by a parameter known as the Poissance [32]. Poissance is a measure of how important space-charge effects are to

[xxii] In the authors' opinion, this is an excellent resource for particle beam propulsion.

beam propagation, and if the current of an un-neutralized beam becomes too large, it will be turned back due to space-charge in the accelerator gap. This imposes a current limit which is plotted in Fig. 27. In practice, accelerator systems are often operated below this limit.

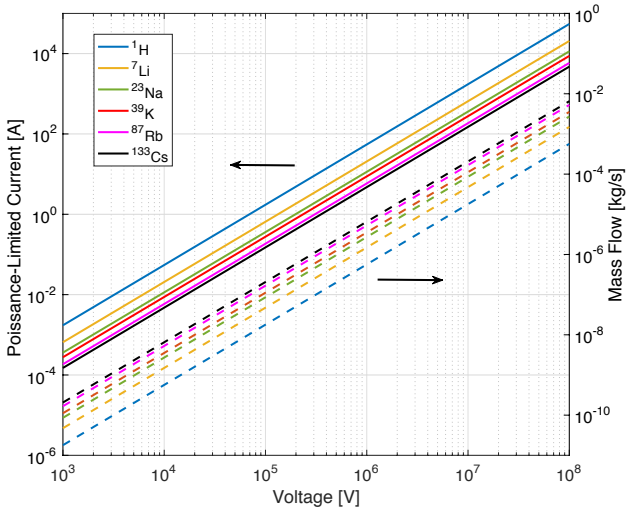

Figure 27: Poissance-limited current and mass flow rate for the alkali metals.

5.3 Neutral Beams

Based on the previous sections, we now consider the type of beam system which can produce both the mass flow rate and high brightness required for neutral beam and self-guided beamed propulsion. To summarize, Sec. 5.1 described how laser cooling can be used to reduce the beam divergence and increase the atomic flux. Although ion extraction and ion optical abberations may increase the beam divergence, laser cooling approaches could be applied after neutralization as well (e.g. [48]). Furthermore, Sec. 5.2 illustrated how space-charge effects limit the beamlet current of high power neutral beams, necessitating a multi-aperture accelerator geometry.

Finally, we must consider the neutralization process. Neutralization requires re-attaching an electron to a positive ion or extracting an electron from a negative ion. For the former process, alkali jet or plasma targets have been demonstrated [101, 102]. For negative ions, alkali jet targets [103] or photo-neutralization [84] are both being pursued. In all cases, neutralization increases the beam divergence through momentum exchange between the target and beam. In particular, photo-neutralization is advantageous since the atomic recoil from electron detachment is very small due to the electron-atom mass ratio. For example, detaching an electron 0.5 eV above threshold results in a cesium recoil of only 0.5 m/s.

A cost-benefit analysis of neutralization approaches and the trade-offs between negative and positive ions is beyond the scope of the present work and will critically affect the feasibility of obtaining high brightness, high energy beams. However, we illustrate in Fig. 28 a nominal beam source concept that could produce the required neutral atom beam. It consists of a laser cooling and compression stage, followed by ionization, ion extraction, acceleration, and neutralization. Ions and neutrals are separated by magnetic field and the atoms are further re-cooled by a laser Doppler system. Grid designs or beam combining techniques will be needed to achieve the appropriate mass flow rates.

The challenge in the final stage will be the short interaction time for laser cooling due to extremely high particle velocity. While an approach based on stimulated cooling may speed the process [104], conventional Doppler cooling rates are limited by the maximum photon scattering rate of $\Gamma/2$, which is of order 30 MHz. For example, a $0.1c$ beam of atoms in a 10 m long optical molasses will only experience 10 scattering events, which is insufficient for full Doppler cooling. Moreover, increased divergence growth during acceleration and neutralization will require longer

interaction times to achieve re-cooling.

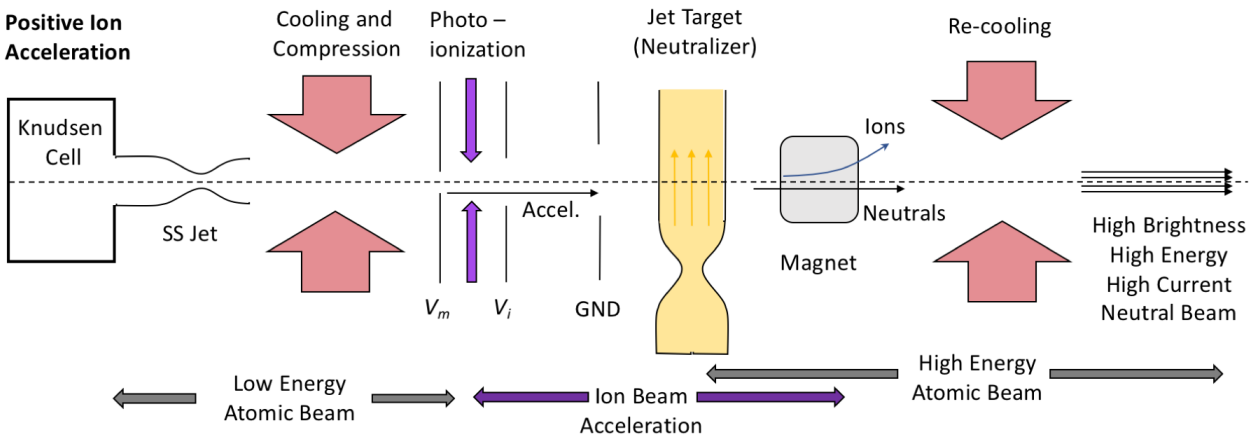

Figure 28: Conceptual high brightness and current neutral beam source based on positive ion beam acceleration, jet target neutralization and re-cooling.

5.4 Technology Development Recommendations

Developing a self-guided beam device capable of executing the missions described in Sec. 3 requires particle beam sources of sufficient brightness and mass flow. Moreover, the particle and laser beam systems must be run at power high and with high attitude stability on a space-based platform. While numerous technological challenges must be overcome, several areas of near-term investigation could greatly enhance to the overall feasibility self-guided beamed propulsion:

1. Development of high flux neutral beam systems for code validation studies and as an atom source for subsequent ionization and acceleration.

2. Study of atomic physics processes relevant to neutral beam sources, ion extraction, neutralization and beam propagation, including: a) cold negative ion production through charge transfer or dissociative attachment, b) cold atom collisions, and c) emittance growth from jet and plasma neutralization collisions.

3. Development of fully-coupled simulation code for modeling of the beam source and propagation. Inclusion of Coulomb interactions (plasma), optical interactions (dipole force, stochastic heating, photo-ionization, photodetachment), and cold and hot collisions are all needed for full end-to-end simulation capability.

4. Development high fidelity system models of the beam source and spacecraft, including power handling, cooling, attitude control, and requirements on spacecraft size, materials, and cost.

5. Theoretical and numerical investigation of beam instabilities, instability growth rates and, if necessary, the development of stabilization approaches exploiting collisions, heating, other other effects.

In addition, the momentum transfer mechanism at the spacecraft was not examined in detail during Phase I. As demonstrated in the Neutralized Drift Compression Experiment, even short bursts of neutral particle impingement can degrade and destroy materials [102]. Therefore, a non-contact method of thrust transfer is highly preferred to direct impact of the neutral particles. A possible solution based on plasma generation was first proposed by Nordley [37] and subsequently analyzed by several authors [105, 82]. In this concept, a laser photo-ionizes the neutral beam, producing a quasi-neutral plasma which is subsequently shielded using magnetic fields. The concept is based on magnetic sails, which have been previously investigated as a method for propulsion [106, 107]. While the necessity of magnetic shielding, even over a short time period of order 1000 sec, is certain to increase the mass of spacecraft subsystems, it may enable deceleration at the host star system [107, 108]. A thorough analysis is recommended in future studies.

6 Conclusion

This study examined a new beamed propulsion concept that exploits mutual self-guiding of a laser and particle beam to overcome and eliminate divergence. The system relies on optical focusing by refractive index gradients and particle trapping by the optical dipole force. In the context of existing propulsion concepts, self-guiding has the potential to disrupt existing trade-offs of both particle and laser beam approaches. A thorough examination of the literature and governing equations demonstrates this concept to be credible.

A wide array of light-matter interactions, and their effect on self-guided beam propagation, were analyzed quantitatively. These studies did not reveal any “show-stoppers", though the benefits of further targeted investigations, such as ion-neutral and cold collision cross sections, were identified. The critical trade-off between the dipole potential depth and stochastic heating rate was also identified. A quantitative analysis of gravitational and centrifugal forces further demonstrated a viable path towards implementation of beamed propulsion systems in cis-lunar space.

The physics of self-guiding were then applied towards missions to Proxima b and to solar gravitational lens point. Optimization of the beam parameters showed a 5 gram payload capability for the originally planned $0.1c$ mission to Proxima b, which is less than initially estimated based on Rayleigh scattering losses. However, a subsequent parametric analysis revealed a strong payload scaling with velocity, and it appears that a somewhat slower $0.044c - 0.075c$ cruise velocity would enable payloads in the range of 1 - 60 kg. These payloads, comparable with recent lightweight spacecraft, constitute a transformational mission capability. This is even more evident when accounting for the transmitter aperture ($1\ \mathrm{m}^2$) and potential efficiency gains using particle beams.

The brightness and mass flow rate were identified as key particle beam parameters that enable the propulsion capabilities described above. While no fundamental limits were identified, current technology is not yet sufficient for breakthrough capabilities. However, a survey of existing technology revealed synergies with disparate research communities and a concerted research efforts to improve future beam systems. The combination of cold atom sources and high power accelerations represents a promising path toward ultra-bright, high power beams, though many challenges remain. These include: source production, divergence growth during acceleration, and neutralization and re-cooling approaches. Developing supporting technologies, such as a cryogenic high density plasma source, will not only enable beamed propulsion concepts but may potentially impact other propulsion technologies, for example gridded ion thrusters.

In conclusion, self-guided beamed propulsion is possible, and may represent a transformational step forward in high velocity propulsion and beamed propulsion capabilities. Important challenges remain, but the basic viability and benefits in payload mass and reduced space infrastructure have been demonstrated through the Phase I analysis. Hopefully, with additional development and innovative approaches to subsystem design, self-guided beams can traverse the inner solar system and lead to the way to the solar gravitational lens point, Proxima b, and the unexplored reaches of our stellar neighborhood.

A Area - Divergence Product

In this section we derive an expression for the minimum achievable spot size of a beam, characterized by its width and local divergence, upon focusing with a linear optical element. Here, linear indicates that the angle change produced by the optic is linearly proportional to the distance from the optical axis, $\Delta\theta \propto r$, and that the angle change is the same for all rays regardless of their local inclination.

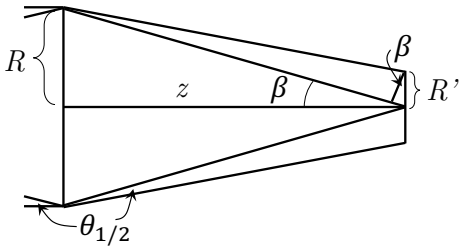

Figure 29: Diagram for spot size derivation.

The problem setup is shown in Figure 29, where the beam radius is given by R and local divergence half-angle $\theta_{1/2}$. The latter is defined at each point on the initial plane, and is the half the maximum angle formed by any two rays passing through a point. Rays, initially parallel to the axis, focus to a point on axis at a distance z from the initial plane. Rays at an angle do *not* focus to a point at z, but remain off-axis by an amount R'. From the angle $\beta = \text{atan}(R/z) \sim R/z$, we can express R' in terms of R and $\theta_{1/2}$. In the small angle approximation, at a distance the maximum beam radius is,

$$R' \approx z\theta_{1/2}. \tag{61}$$

However, at the same time the beam half-angle is,

$$\theta_{1/2}{}' = \beta = \text{atan}\left(\frac{R}{z}\right) \approx \frac{R}{z}, \tag{62}$$

which is most easily observed on axis. As a result, the product of R' and $\theta_{1/2}{}'$ is,

$$R'\theta_{1/2}{}' = (z\theta_{1/2})\left(\frac{R}{z}\right) = \theta_{1/2}R = \text{constant}. \tag{63}$$

It is trivially shown that the area-divergence product is also conserved. If we consider the maximum distance L to which we can focus to a spot A_{sc}, we can then write from the area-divergence product,

$$A_{sc} = \Pi/\Omega = \frac{\Pi}{\pi(R_t/L)^2}, \tag{64}$$

and solving for the maximum distance,

$$L = \sqrt{\frac{A_{sc}A_t}{\Omega}}. \tag{65}$$

Finally, we note that if $\beta < \theta_{1/2}$, the beam size will not be reduced from the initial value of R but expand, albeit more slowly than before.

B Paraxial Wave Equation Derivation

In this section, we derive the paraxial wave equation beginning with the macroscopic Maxwell equations [109, 30, 110]. For a non-magnetic, purely dielectric medium with no free currents, they read,

$$\nabla \cdot (\epsilon E) = 0 \tag{66}$$
$$\nabla \cdot B = 0 \tag{67}$$
$$\nabla \times E = -\frac{\partial B}{\partial t} \tag{68}$$
$$\nabla \times B = \frac{\partial (\epsilon E)}{\partial t} \tag{69}$$

where $\epsilon = \epsilon_0 \eta^2$ is the permittivity of the medium. First, we derive the wave equation by the usual method of taking the curl of Eq. 69c and using the vector Laplacian identity, we arrive at,

$$\nabla \times \nabla \times \mathbf{E} = -\nabla^2 \mathbf{E} + \nabla(\nabla \cdot \mathbf{E}) = -\frac{\partial}{\partial t}(\nabla \times \mathbf{B}). \tag{70}$$

In a vacuum, the divergence of $\mathbf{E}$ would be zero, but since the media is inhomogeneous, we must replace it by expanding Eq. 66,

$$\nabla \cdot (\epsilon \mathbf{E}) = \epsilon \ \nabla \cdot \mathbf{E} + \mathbf{E} \cdot \nabla \epsilon \tag{71}$$
$$\nabla \cdot \mathbf{E} = -\mathbf{E} \nabla \epsilon / \epsilon. \tag{72}$$

Combining this result with Eq. 69, the exact wave equation in media can be written,

$$\nabla^2 \mathbf{E} - \frac{\eta^2}{c^2} \frac{\partial^2 \mathbf{E}}{\partial t^2} = -\nabla[\mathbf{E} \cdot \nabla(\ln(\epsilon))] \tag{73}$$

where we have assumed that ϵ is time independent and $\eta^2 = (\epsilon \mu_0)^{-1}$. Compared with the free-space wave equation, both the index of refraction and a polarization dependent nonlinear source term have been introduced. Shortly, we will show the latter to be second order in $\delta\epsilon$.

We now consider a time-harmonic and linearly polarized electric field, which can be described by the $\mathbf{E}(\mathbf{r}) = e^{i\omega t}\hat{\imath}$, where $\mathbf{E}(\mathbf{r})$ is the spatially-varying field amplitude and $\hat{\imath}$ is the x-component unit vector. Substituting into the wave equation, we obtain a scalar wave equation,

$$\nabla^2 E + k^2 E = -\nabla \left(E \frac{\partial \ln(\epsilon)}{\partial x} \right), \tag{74}$$

where $k^2 = \eta^2 k_0^2$ is the propagation constant in media and $\omega/c = k$. The first term in Eq. 74 gives rise to diffraction, while the second describes guiding by refractive index variations. The term on the right-hand side introduces a three-dimensional effect through the partial derivative along the beam polarization direction. We now show that this term is second order in the smallness parameter $\delta\epsilon$. For a beam of transverse dimension Δ much larger than the wavelength, the first term is of order E_0/Δ^2, while the second term is or order $k^2 \delta\epsilon \sim E_0 \delta\epsilon \lambda^{-2}$. In a single mode waveguide, these two contributions are of similar order, and thus $(\lambda/\Delta)^2 \sim \delta\epsilon$. The term on the right hand side is seen to be of order $E_0 \delta\epsilon/\Delta^2 \sim E_0 (\delta\epsilon)^2/\lambda^2$. For the dilute medium we consider

here, $\delta\epsilon << 1$ and indeed for many applications $\delta\epsilon$ is of order 10^{-10}. Thus, to good approximation, the RHS of Eq. 74 can be set equal to zero. The result constitutes the scalar Helmholtz equation for the electric field amplitude.

Finally, we wish to consider propagation of a highly directional, nearly collimated ("paraxial") beam. We therefore express the electric field as having primarily a plane wave character, $E = \bar{E}e^{ik_0 z}$, the so-called paraxial approximation. Substituting into the Helmholtz equation, we find,

$$\nabla_\perp^2 \bar{E} + 2ik_0 \frac{\partial \bar{E}}{\partial z} + \frac{\partial^2 \bar{E}}{\partial z^2} + k_0^2(\eta^2 - 1)\bar{E} = 0. \tag{75}$$

If the beam is large compared to λ, its spatial profile changes rather slowly by diffraction. Consequently, by scaling arguments we find the second order z-derivative to be small compared with the other transverse second derivatives (perpendicular to the axis: $\nabla_\perp$). Setting $\partial^2/\partial z^2$ equal to zero, we arrive at an approximation to the scalar wave equation known as the paraxial Helmholtz equation,

$$\nabla_\perp^2 \bar{E} + 2ik_0 \frac{\partial \bar{E}}{\partial z} + k_0^2(\eta^2 - 1)\bar{E} = 0. \tag{76}$$

References

[1] Agnlada-Escude, Guillem and Amado, Pedro J. and Barnes, John and Others. A terrestrial planet candidate in a temperate orbit around Proxima Centauri. *Nature*, 536(7617):437–440, 2016.

[2] Ribas, I. and Tuomi, M. and Reiners, A. and Others. A candidate super-Earth planet orbiting near the snow line of Barnard's star. *Nature*, 563(7731):365–368, 2018.

[3] Millis, Marc G and Greason, Jeff and Stevenson, Rhonda. Breakthrough Propulsion Study: Assessing Interstellar Flight Challenges and Prospects. Technical report, Tau Zero Foundation, NASA Report Number HQ-E-DAA-TN60290, 2018.

[4] Parkin, Kevin L G. The Breakthrough Starshot System Model. *arXiv preprint*, 2018.

[5] Lubin, Philip. A Roadmap to Interstellar Flight. *JBIS - Journal of the British Interplanetary Society*, 69:40–72, 2016.

[6] Breakthrough Starshot Foundation, https://breakthroughinitiatives.org/Initiative/3..

[7] Hundred Year Starship Project, http://100yss.org/..

[8] Adams, Robert B. and Cassibry, Jason and Bradley, D. and Fabisinski, Leo and Statham, G. Developing the Pulsed Fission-Fusion (PuFF) Engine. *50th AIAA/ASME/SAE/ASEE Joint Propulsion Conference*, 2014. AIAA Propulsion and Energy Forum (AIAA 2015-3520).

[9] LaPointe, M. and Adams, R. and Cassibry, J. and Zweiner, M. and Gilland, J. Preliminary Analysis of the Gradient Field Imploding Liner Fusion Propulsion Concept. *2018 Joint Propulsion Conference'*, Cincinnati, Ohio, 2018. AIAA Propulsion and Energy Forum (AIAA 2018-4953).

[10] Thomas, Stephanie J and Paluszek, Michael A. and Cohen, Samuel A. and Glasser, Alexander. Nuclear and Future Flight Propulsion - Modeling the Thrust of the Direct Fusion Drive. *2018 Joint Propulsion Conference'*, Cincinnati, Ohio, 2018. AIAA Propulsion and Energy Forum (AIAA 2018-4769).

[11] Paluszek, Michael A. and Thomas, Stephanie J. and Hinterman, Eric and Nagai, Yukino and Peng, Lisa and Walsh, Audrey and Cohen, Samuel A. and Gaitan, Gabriel and Ham, Eric. Space Nuclear Power Systems - Direct Fusion Drive. *International Energy Conversion Engineering Conference*, Cincinnati, Ohio, 2018. AIAA Propulsion and Energy Forum (AIAA 2018-4974).

[12] Razin, Yosef S. and Pajer, Gary and Breton, Mary and Ham, Eric and Mueller, Joseph and Paluszek, Michael and Glasser, Alan H. and Cohen, Samuel A. A direct fusion drive for rocket propulsion. *Acta Astronautica*, 105(1):145–155, 2014.

[13] Brophy, John R and Polk, James E and Goebel, Dan M. Development of a 50,000-s, Lithium-fueled, Gridded Ion Thruster. *35th International Electric Propulsion Conference*, :1–7, 2017.

[14] Lubin, Philip and Brashears, Travis and Hughes, Gary and Zhang, Qicheng and Griswald, Janelle and Kosmo, Kelly. Effective Planetary Defense using Directed Energy DE-STARLITE. *4th IAA Plantary Defense Conference*, number April, Frascati, Roma, Italy, 2015.

[15] Askar'yan, G.A. Effects of the Gradient of a Strong Electromagnetic Beam on Electrons and Atoms. *Soviet Physics JETP*, (15):1088–1090, 1962.

[16] Yu.L. Klimontovich and S.N. Luzgin. The possibility of combined self-focusing of atomic and light beams. *Pis'ma Zh. Eksp. Teor. Fiz.*, 30(645), 1979.

[17] Saffman, M. Self-Induced Dipole Force and Filamentation Instability of a Matter Wave. *Physical Review Letters*, 81(1):65–68, 1998.

[18] Tesio, E and Robb, G R M and Ackemann, T and Firth, W J and Oppo, G. Kinetic Theory for Transverse Optomechanical Instabilities. *Physical Review Letters*, 112(043901):1–5, 2014.

[19] Tesio, E and Robb, G R M and Ackemann, T and Firth, W J and Oppo, G. Dissipative solitons in the coupled dynamics of light and cold atoms. *Optics Express*, 21(22):26144–26149, 2013.

[20] Labeyrie, G and Tesio, E and Gomes, P M and Oppo, G and Firth, W J and Robb, G R M and Arnold, A S and Kaiser, R and Ackemann, T. Optomechanical self-structuring in a cold atomic gas. *Nature Photonics*, 8(4):321–325, 2014.

[21] Nordley, Gerald D and Crowl, Adam James. Mass Beam Propulsion, An Overview. *Journal of the British Interplanetary Society*, 68, 2015.

[22] Sänger, E. Zur Theorie der Photonenraketen. *Probleme der Weltraumforschung, International Astronautical Federation, Zürich*, 1954.

[23] Sänger, E. Strahlungsquellen für Photonenstrahlantriebe. *Astronautica Acta*, 5:15–25, 1959.

[25] Marx, G. Interstellar Vehicle Propelled by Terestrial Laser Beam. *Nature*, 211:22–23, 1966.

[25] Marx, G. Interstellar vehicle propelled by terrestrial laser beam. *Nature*, 211(5044):22–23, 1966.

[26] Redding, J. L. Interstellar Vehicle Propelled by Terrestrial Laser Beam. *Nature*, 213(Feb.):588–589, 1967.

[28] Forward, R. Roundtrip interstellar travel using laser-pushed lightsails. *Journal of Spacecraft and Rockets*, 21(2):187–195, 1984.

[28] Forward, Robert L. Roundtrip Interstellar Travel Using Laser-Pushed Lightsails. *Journal of Spacecraft and Rockets*, 21(2):187–195, 1984.

[29] McClelland, Jabez J. Nanofabrication via Atom Optics. *Handbook of Nanostructured Materials and Nanotechnology*, chapter Nanofabric. Academic Press, 2000.

[30] Born, Max and Wolf, Emil. *Principles of Optics: Electromagnetic Theory of Propagation, Interference and Diffraction of Light*. CUP Archive, 2000.

[31] Klemperer, O. *Electron Optics, 2nd ed.*. Cambridge University Press, London, 1953.

[32] Forrester, A. T. *Large Ion Beams*. Wiley Interscience, 1988.

[33] Wolf, B. *Handbook of Ion Sources*. CRC Press, 1995.

[34] Kim, J.A. and Littlejohn, R.G. Entropy and Emittance of Particle and Photon Beams. *Proceedings Particle Accelerator Conference*, 1995.

[35] Forward, R.L. Starwisp: an Ultralight Interstellar Probe. *J. Spacecraft and Rockets*, 22:345–350, 1985.

[36] Siegman, Anthony E. *Lasers*. University Science Books, 1986.

[37] Nordley, G.D. Particle Beam Propulsion and Two-Way EML Propulsion. In R.H. Frisbee,

editors, *JPL D-10673: NASA/OAST Fourth Advanced Space Propulsion Workshop*, pages 473, Jet Propulsion Laboratory, Pasadena CA, 1993.

[38] Kare, Jordin T. High-acceleration Micro-scale Laser Sails for Interstellar Propulsion. Technical report, NASA Institute for Advanced Concepts, Phase I Final Report, 2002.

[39] Nordley, G.D. Interstellar Probes Propelled by Self-steering Momentum Transfer Particles. In IAA-01-IAA.4.1.05, Paper, editors, *52nd International Astronautical Congress*, Toulouse, France, 2001.

[40] Winglee, R M and Ziemba, T and Giersch, L and Prager, J and Roberson, B R and Carscadden, J. Advances in High Power Beamed Plasma Propulsion. *38th Plasmadynamics and Lasers Conference*, number June, pages 98195–98195, Miami, FL, 2007.

[41] Metcalf, H.J and van der Straten, P. Laser Cooling and Trapping of Atoms. *Journal of the Optical Society of America B*, 6(11):2020, 1989.

[42] Phillips, William D. Laser cooling and trapping of neutral atoms*. *Reviews of Modern Physics*, 70(3):721–741, 1998.

[43] Lett, P. D. and Phillips, W. D. and Rolston, S. L. and Tanner, C. E. and Watts, R. N. and Westbrook, C. I. Optical molasses. *Journal of the Optical Society of America B*, 6(11):2084, 1989.

[44] Castin, Y. and Wallis, H. and Dalibard, J. Limit of Doppler cooling. *Journal of the Optical Society of America B*, 6(11):2046, 1989.

[45] Minogin, V. G. and Letokhov, V. S. *Laser Light Pressure on Atoms*. Gordon and Breach, New York, 1987.

[46] Grimm, Rudolf and Weidemuller, Matthias and Ovchinnikov, Yurii B. Optical dipole traps for neutral atoms. *Advances In Atomic, Molecular, and Optical Physics*, 42:95–107, 2000.

[47] Dalibard, Jean. Collisional dynamics of ultra-cold atomic gases. *Proceedings of the International School of Physics - Enrico Fermi*, 321:14, 1999.

[48] Lam, J.F. and McFarlane, R.A. and Palmer, A.J. and Steel, D.G. and Turley, R.S. Experimental and Theoretical Studies of Laser Cooling and Emittance Control of Neutral Beams. Technical report, AFOSR TR 87-0339, Malibu, CA, 1987.

[49] Bjorkholm, J.E. and Freeman, R.R. and Ashkin, A. and Pearson, D.B. Observation of Focusing of Neutral Atoms by the Dipole Forces of Resonance-Radiation Pressure. *Physical Review Letters*, 41:1361, 1978.

[50] Saffman, Mark and Skryabin, Dmitry V. Spatial Solitons. In Rhodes, W.T., editors, *Spatial Solitons*, chapter Coupled Pr. Springer-Verlag, Berlin Heidelberg, 2001.

[51] Khaykovich, L. and Schreck, F. and Ferrari, G. and Bourdel, T. and Cubizolles, J. and Carr, L. D. and Castin, Y. and Salomon, C. Formation of a matter-wave bright soliton. *Science*, 296(5571):1290–1293, 2002.

[52] Saleh, Bahaa E A and Teich, Malvin Carl. *Introduction to Photonics*. John Wiley & Sons, Inc., 1991.

[53] Boyd, Robert W. *Nonlinear Optics*. Elsevier Science, 2013.

[54] Couairon, A and Mysyrowicz, A. Femtosecond filamentation in transparent media. *Physics Reports*, 441:47–189, 2007.

[55] Steck, Daniel Adam. *Quantum and Atom Optics*. 2018.

[56] Ashkin, A. Applications of laser radiation pressure.. *Science (New York, N.Y.)*, 210(4474):1081–1088, 1980.

[57] Ashkin, A. Motion of atoms in a radiation trap. *Physical Review A*, 21(5):1606–1617, 1980.

[58] Ashkin, A. Optical trapping and manipulation of neutral particles. *Proc. Natl. Acad. Sci.*, 94(May):4853–4860, 1997.

[59] Milonni, Peter W. and Boyd, Rober. Momentum of Light in a Dielectric Medium. *Advances in Optics and Photonics*, 2:519–553, 2010.

[60] Barnett, Stephen M and Loudon, Rodney. On the electromagnetic force on a dielectric medium. *Journal of Physics B: Atomic, Molecular and Optical Physics*, 39:S671–S684, 2006.

[61] Miller, J.D. and Cline, R.A. and Heinzen, D.J. Far-off-resonance optical trapping of atoms. *Physics Review A*, 47(6):4567–4570, 1993.

[62] Takekoshi, T and Knize, R J. CO2 laser trap for cesium atoms. *Optics Letters*, 21(1):77–79, 1996.

[63] Miles, Richard B and Lempert, Walter R and Forkey, Joseph N. Laser Rayleigh scattering. *Meas. Sci. Technol.*, 12:33–51, 2001.

[64] Wang, C. and Richardson, J. D. Determination of the solar wind slowdown near solar maximum. *Journal of Geophysical Research: Space Physics*, 108(A2), 2003.

[65] Weiner, John and Bagnato, Vanderlei S. and Zilio, Sergio and Julienne, Paul S. Experiments and theory in cold and ultracold collisions. *Reviews of Modern Physics*, 71(1):1–85, 1999.

[66] Inguscio, M and Stringari, S and Wieman, C E. *Bose-Einstein Condensation in Atomic Gases*. Societa' italiana di Fisica, Italy, 1999.

[67] Mainfray, G. and Manus, C. Multiphoton ionization of atoms. *Advances in Electronics and Electron Physics*, 36:57–152, 1974.

[68] Bebb, H. Barry. Theory of three-photon ionization of the alkali atoms. *Physical Review*, 153(1):23–28, 1967.

[69] Chang, T.N. and Poe, Robert T. Two- and three-photon ionization of hydrogen and lithium. *Physical Review A*, 16(2):606–612, 1977.

[70] Morellec J, Normand D and Petite G. Morellec J, Normand D and Petite G 1976 Phys. Rev. A 14 300.12 -. *Physical Review A*, 14:300–12, 1976.

[71] Einstein, A. Explanation of the perihelion motion of mercury from the general theory of relativity. *Sitzungsber. Preuss. Akad. Wiss. Berlin*, :831–839, 1915.

[72] Fini, John M. Design of large-mode-area amplifier fibers resistant to bend-induced distortion. *Journal of the Optical Society of America B*, 24(8):1669, 2007.

[73] Chiang, K.S. Analysis of optical fibers by the effective-index method. *Applied Optics*, 25(3):348–354, 1986.

[74] Tsao, Charles. *Optical Fibre Waveguide Analysis*. Oxford University Press, Oxford, 1992.

[75] Gloge, D. Weakly guiding fibers. *Applied Optics*, 10(11):2252–2258, 1971.

[76] Sacks, Lia W. and Blaurock, Carl and Dewell, Larry D. and Tajdaran, Kiarash and Liu, Kuo-

Chia and Collins, Christine and West, Garrett J. and Ha, Kong Q. and Bolcar, Matthew R. and Crooke, Julie A. and Hylan, Jason E. and Bell, Raymond M. Preliminary jitter stability results for the large UV/optical/infrared (LUVOIR) surveyor concept using a non-contact vibration isolation and precision pointing system. *Proc. SPIE 10698, Space Telescopes and Instrumentation 2018:Optical, Infrared and Millimeter Wave*, number July 2018, Austin, TX, 2018.

[77] Benford, J. Starship Sails Propelled by Cost-Optimized Directed Energy. *Journal of the British Interplanetary Society*, 66(85), 2013.

[78] Wright, W. P. and Ferrer, P. Electric micropropulsion systems. *Progress in Aerospace Sciences*, 74:48–61, 2015.

[79] Tsao, C. C. and Wang, Y. and Weiner, J. and Bagnato, V. S. Optical collimation and compression of a thermal atomic beam. *Journal of Applied Physics*, 80(1):8–14, 1996.

[80] Kime, L. and Fioretti, A. and Bruneau, Y. and Porfido, N. and Fuso, F. and Viteau, M. and Khalili, G. and Šantić, N. and Gloter, A. and Rasser, B. and Sudraud, P. and Pillet, P. and Comparat, D. High-flux monochromatic ion and electron beams based on laser-cooled atoms. *Physical Review A - Atomic, Molecular, and Optical Physics*, 88(3), 2013.

[81] ten Haaf, G and Wouters, S H W and Mutsaers, P H A and Vredenbregt, E J D. Cavity-enhanced photoionization of an ultracold rubidium beam for application in focused ion beams. *Physical Review A*, 053412:1–12, 2017.

[82] Landis, G. A. Interstellar Flight by Particle Beam. *STAIF Conference on Innovative Transportation Systems for Exploration of the Solar System and Beyond*, pages 0–3, Albuquerque, NM, 2001.

[83] McCormick, K., S. and Fiedler, G. and Kocsis, J. and Schweinzer and Zoletnik, S. Edge density measurements with a fast Li beam probe in tokamak and stellarator experiments. *Fusion Engineering and Design*, :125–134, 1997.

[84] Simonin, A and Agnello, R and Bechu, S and Bernard, J M and Blondel, C and Boeuf, J P and Bresteau, D and Cartry, G and Chaibi, W and Drag, C and Duval, B P and Esch, H P L De and Fubiani, G and Furno, I and Grand, C and Guittienne, Ph and Howling, A and Jacquier, R and Marini, C and Morgal, I. Negative ion source development for a photoneutralization based neutral beam system for future fusion reactors. *New Journal of Physics*, 18:125005, 2016.

[85] Turyshev, Slava G. and B. G. Andersson. The 550-au mission: a critical discussion. *Monthly Notices of the Royal Astronomical Society*, 341.2:577–582, 2003.

[86] Hadley, G R. Transparent boundary condition for the beam propagation method. *IEEE Journal of Quantum Electronics*, 28(1):363–370, 1992.

[87] Cai, Chunpei and Boyd, Iain D. Collisionless Gas Expanding into Vacuum. *Journal of Spacecraft and Rockets*, 44(6):1326–1330, 2007.

[88] Cai, Long and White, Ralph E. Model Reduction via Proper Orthogonal Decomposition for the Lithium Ion Battery. *ECS Transactions*, :13–26, 2008.

[89] Lubin, Philip and Hughes, Gary B. and Bible, Johanna and Johansson, Isabella. Directed energy for relativistic propulsion and interstellar communications. *JBIS - Journal of the British Interplanetary Society*, 68(5-6):172–182, 2015.

[90] Chu, J. O. and Wood, Carol F. and Flynn, G. W. and Weston, Ralph E. Counting vibrational

quanta with a diode laser probe: Bending and stretching excitation in CO2 caused by collisions with hot atoms from excimer laser photolysis. *The Journal of Chemical Physics*, 81(12):5533, 1984.

[91] Berthoud, P and Fretel, E and Thomann, P. Bright, slow, and continuous beam of laser-cooled cesium atoms. *Physical Review A*, 60(6):4241–4244, 2000.

[92] Balykin, V I and Melentiev, P N and Mancini, Stefano and Bonifacio, Rodolfo. Strong Velocity Compression of a Supersonic Atomic Beam Using Moving Optical Molasses. *Europhysics Letters*, 17(5):393–399, 1992.

[93] Lamporesi, G. and Donadello, S. and Serafini, S. and Ferrari, G. Compact high-flux source of cold sodium atoms. *Review of Scientific Instruments*, 84(6), 2013.

[94] Sheehy, B. and Shang, S. Q. and van der Straten, P. and Metcalf, H. Collimation of a rubidium beam below the Doppler limit. *Chemical Physics*, 145(2):317–325, 1990.

[95] Knuffman, B and Steele, A V and McClelland, J J. Cold atomic beam ion source for focused ion beam applications. *Journal of Applied Physics*, 114:44303, 2013.

[96] Wouters, S H W and Haaf, G and Notermans, R P M J W and Debernardi, N and Mutsaers, P H A. Performance predictions for a laser-intensified thermal beam for use in high-resolution focused-ion-beam instruments. *Physical Review A*, 90:063817, 2014.

[97] van der Geer, S. B. and Reijnders, M. P. and de Loos, M. J. and Vredenbregt, E. J. D. and Mutsaers, P. H. A. and Luiten, O. J. Simulated performance of an ultracold ion source. *Journal of Applied Physics*, 102:94312, 2007.

[98] Hemsworth, R. S. and Boilson, D. and Blatchford, P. and Palma, M. Dalla and Chitarin, G. and De Esch, H. P.L. and Geli, F. and Dremel, M. and Graceffa, J. and Marcuzzi, D. and Serianni, G. and Shah, D. and Singh, M. and Urbani, M. and Zaccaria, P. Overview of the design of the ITER heating neutral beam injectors. *New Journal of Physics*, 19(2), 2017.

[99] Anda, G. and Bencze, A. and Berta, M. and Dunai, D. and Hacek, P. and Krbec, J. and Rafy, D. and Krizsansczi, T. and Batts, S. and Ilkei, T. and Kiss, I. G. and Veres, G. and Zoletnik, S. Lithium beam diagnostic system on the COMPASS tokamak. *Fusion Engineering and Design*, 108:1–6, 2016.

[100] Brix, M. and Dodt, D. and Korotkov, A. and Morgan, P. and Dunai, D. and Fischer, R. and Meigs, A. and Nedzelskiy, I. S. and Schweinzer, J. and Vince, J. and Zoletnik, S. and Contributors, JET-EFDA. Upgrade of the lithium beam diagnostic at JET. *Review of Scientific Instruments*, 81(10):10D733, 2010.

[101] Franzen, P. and Falter, H. D. and Fantz, U. and Kraus, W. and Berger, M. and Christ-Koch, S. and Fröschle, M. and Gutser, R. and Heinemann, B. and Hilbert, S. and Leyer, S. and Martens, C. and McNeely, P. and Riedl, R. and Speth, E. and Wünderlich, D. Progress of the development of the IPP RF negative ion source for the ITER neutral beam system. *Nuclear Fusion*, 47(4):264–270, 2007.

[102] Seidl, P. A. and Barnard, J. J. and Feinberg, E. and Friedman, A. and Gilson, E. P. and Grote, D. P. and Ji, Q. and Kaganovich, I. D. and Ludewigt, B. and Persaud, A. and Sierra, C. and Silverman, M. and Stepanov, A. D. and Sulyman, A. and Treffert, F. and Waldron, W. L. and Zimmer, M. and Schenkel, T. Irradiation of materials with short, intense ion pulses at NDCX-II. *Laser and Particle Beams*, 35(2):373–378, 2017.

[103] Grisham, L. R. Lithium jet neutralizer to improve negative ion neutral beam performance. *AIP Conference Proceedings*, 1097(2007):364–373, 2009.

[104] Aspect, A. and Dalibard, J. and Heidmann, A. and Salomon, C. and Cohen-Tannoudji, C. Cooling Atoms with Stimulated Emission. *Physical Review Letters*, 57:1688, 1986.

[105] Andrews, Dana G. Cost considerations for interstellar missions. *JBIS - Journal of the British Interplanetary Society*, 49(4):123–128, 1996.

[106] Winglee, R. M. and Slough, J. and Ziemba, T. and Goodson, a. Mini-Magnetospheric Plasma Propulsion: Tapping the energy of the solar wind for spacecraft propulsion. *Journal of Geophysical Research*, 105(A9):21067, 2000.

[107] Andrews, Dana G. and Zubrin, Robert M. Magnetic Sails and Interstellar Travel. *IAP Paper IAF-88-5533*, Bangalore, Indian, 1988.

[108] Greason, J. Missions Enabled by Plasma Magnet Sails. *TVIW, Huntsville AL. https://tviw.us/2017- presentation-video-archive/, Presentation "10."*, 2017.

[109] Jackson, John David. *Classical Electrodynamics*. Wiley, New York, NY, 3rd ed. edition, 1998.

[110] Landau, L D and Lifshitz, E M and Pitaevskii, L P. *Electrodynamics of Continuous Media*. Oxford: Heinemann, 1984.